

# We are IntechOpen, the world's leading publisher of Open Access books Built by scientists, for scientists

6,900

Open access books available

186,000

International authors and editors

200M

Downloads

Our authors are among the

154

Countries delivered to

TOP 1%

most cited scientists

12.2%

Contributors from top 500 universities



WEB OF SCIENCE™

Selection of our books indexed in the Book Citation Index  
in Web of Science™ Core Collection (BKCI)

Interested in publishing with us?  
Contact [book.department@intechopen.com](mailto:book.department@intechopen.com)

Numbers displayed above are based on latest data collected.  
For more information visit [www.intechopen.com](http://www.intechopen.com)



# Salt Tectonics of the Lisan Diapir Revealed by Synthetic Aperture Radar Images

Damien Closson<sup>1</sup>, Najib Abou Karaki<sup>2</sup>, Nada Milisavljević<sup>3</sup>,  
Frédéric Hallot<sup>3</sup>, and Marc Acheroy<sup>3</sup>

<sup>1</sup>*Signal and Image Centre. Avenue de la Renaissance 30, Brussels 1000,*

<sup>2</sup>*University of Jordan, Environmental and Applied Geology Department, Amman,*

<sup>3</sup>*Signal and Image Centre. Avenue de la Renaissance 30, Brussels 1000,1*

<sup>1,3</sup>*Belgium*

<sup>2</sup>*Jordan*

## 1. Introduction

### 1.1 General setting

In the Oligocene, the Africa-Arabia plate broke up separating Arabia and Sinai as individual plate and sub-plate. Since then, the Arabian plate moves northward along the Jordan - Dead Sea Transform (JDST) fault more rapidly than the Sinai sub-plate. This left-lateral strike slip movement (Figure 1) had displaced Early Miocene dykes across the fault zone up to 100 km (Quennell, 1958; Freund et al., 1970; Garfunkel et al., 1981) and had resulted in the development of rhomb-shaped grabens such as the Dead Sea pull-apart basin along the main fault (Figure 1, inset).

The Dead Sea Basin is the largest pull-apart along the JDST fault. It is about 150 km x 15 km. Repeated structural subsidence resulted in the accumulation of sedimentary rocks as much as 10 km thick (Garfunkel and Ben Avraham, 1996). Inside the basin, two sets of faults, both oriented roughly N-S, can be recognized (Figure 1, inset). The first set is the extension of the northern and southern segments of the JDST fault, forming the pull-apart basin (Ben Avraham, 1997; Garfunkel, 1997). These faults are accommodating most of the horizontal motion of the JDST fault. The second set is constituted by the transverse faults, oriented NNW-SSE, that cross obliquely the basin at interval of 20-30 km. Between these faults, the basin infill is slightly back-tilted toward the south with no large deformations (Gardosh et al., 1997; Ben Avraham, 1997; Al Zoubi and ten Brink, 2001). Strong deformations are known only near the diapirs formed by the salt of the Sedom Formation (2 km thick). The Sedom formation formed from the late Miocene to the Pliocene (5.3 - 2.5 Ma). It is composed of 75% rocksalt which arrived via marine ingression from the Mediterranean and Red Seas. This flooding has ceased, however, with a rise of intrusive rock in the Araba and Jezreel valleys (Figure 1). The rocksalt is interbedded with anhydrite and gypsum, reddish dolomite, silt, sand and clay. Since the early Miocene, the center of sedimentary deposition existed where the Lisan area (Figure 1, inset) is currently located.

During the Pliocene excessive accumulation of sediment caused a diapiric upward movement of accumulated lower-density sediment to begin, thus forming several salt

domes structures. Among these diapirs, the one located under the Lisan area is the largest (Figure 1, inset; Figure 2) and constitutes the element under investigation.

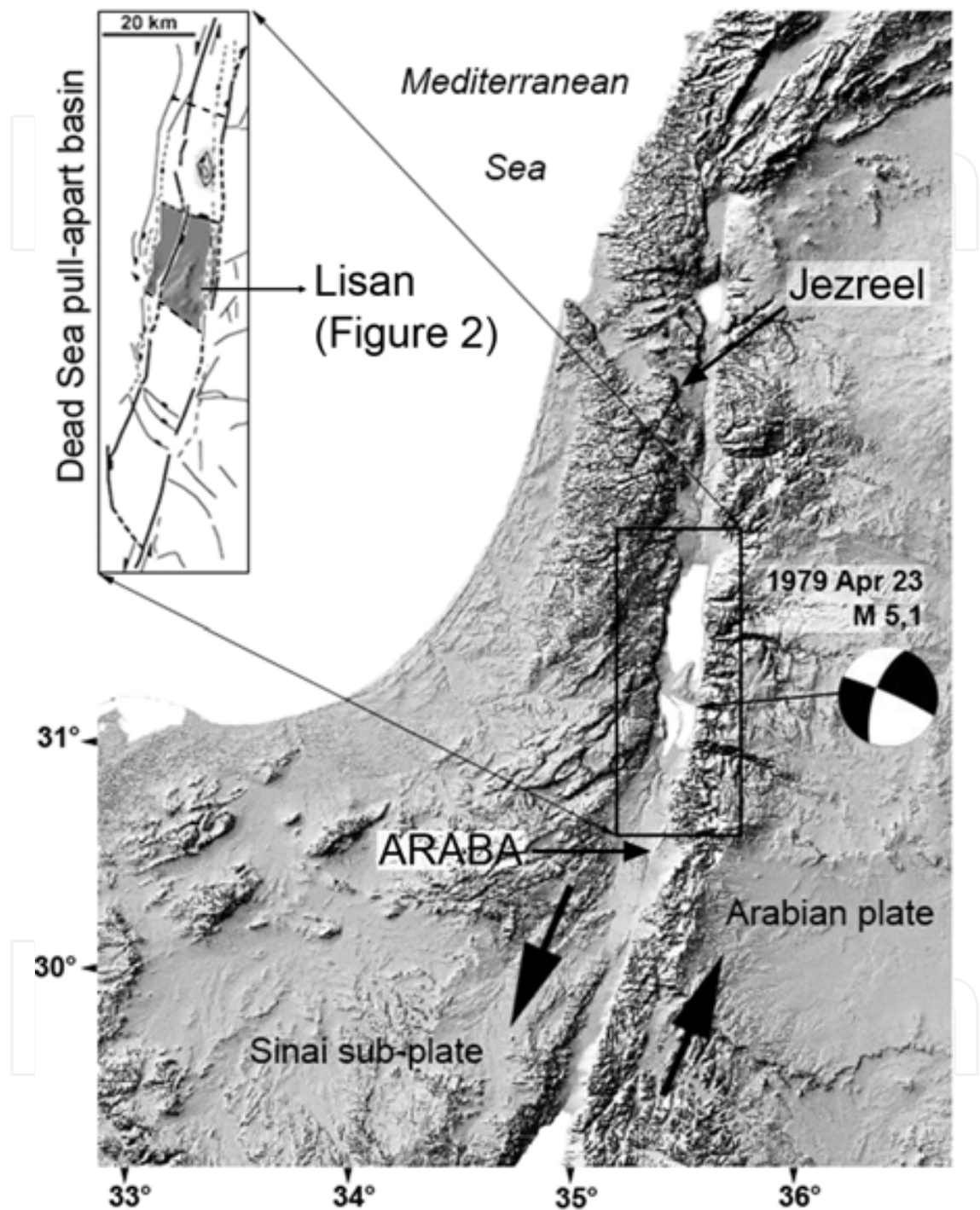


Fig. 1. The area of interest in its global setting. The shaded relief image (Space Radar Topography Mission, Feb. 2000) focuses on the Jordan - Dead Sea transform fault zone. Inset shows the main tectonic elements of the Dead Sea pull-apart basin (after Ben Avraham, 1997; Ben Avraham and Lazar, 2006). The focal mechanisms associated with the earthquake of April 23, 1979 (Arieh et al., 1982) is representative of all focal mechanisms calculated on a fault plane compatible with the general direction of the Jordan - Dead Sea Transform.

## 1.2 Goal of this work

This chapter presents and discusses ground surface displacements affecting the Lisan area. The displacement fields have been investigated owing to the processing of 27 radar images acquired by C- and L-band sensors onboard satellites (ALOS, ENVISAT, and ERS 1&2). The time period concerned ranges from 1992 to 2008. Uplift and subsidence have been mapped and analyzed inside a geographical information system. Two “tandem” pairs of ERS 1&2 satellite have been processed to create two digital surface models of the studied area. It compensates for the lack of updated information in the fields of topography and geomorphology. The work on these models targeted the mapping of lineaments, the detection drainage pattern anomalies, the definition of the drainage texture, and the extraction of topographic features which can be explained by structural or stratigraphic conditions.

## 2. Background

### 2.1 Tectonic setting

At regional scale, the Lisan appears to be a structurally complex rhomboid-shaped tectonic unit (Figure 2 inset). Parallel and curvilinear faulted zones define either elongated or almond-shaped grabens on its eastern and western sides (Lynch Strait, Ghor Al Mazra’a, Ghor Al Haditha – Figure 2). North and south, the Lisan is respectively bounded by a faulted zone separating the northern to the southern basin and by a discontinuity (Figure 2, inset, dashed line) representing the edge of the Lisan salt diapir (Ben Avraham and Lazar, 2006).

The top of the salt dome (Figure 2) is estimated to be at 125 m below the surface based on drill holes that have penetrated over 100 m of deformed lake deposits (Neev and Emery, 1967; Zak, 1967, Bender, 1974). With respect to the Lisan peninsula, the main out-cropping formation is the Lisan Marl (chalk, marly chalk, gypsum, salt and conglomerate). Based on photogeological interpretation and field observations, Sunna (1986) subdivided this formation into two Members (Lower and Upper) while Bartov et al. (2006) subdivided the marls into three Members (Lower: 60-40 Kyr, Middle: 40-32 Kyr, and Upper: 32-15 Kyr) based on U-Th dating method.

Al Zoubi and ten Brink (2001) used seismic data correlated to several deep wells (Zak, 1967; Bender, 1974) to determine the size of the elongated Lisan diapir: 13 km x 10 km x 7.2 km (Figure 2, top salt contours). Its geometry is tectonically controlled. At the ground surface, fault escarpments of 20 to 40 m (Figure 3, see location on Figure 2) indicate the limit of the former peninsula. On the western side it is difficult to determine the orientation of individual faults due to insufficient exposure caused by the setting up of salt pans (Figure 2) in the 1990s. Bartov et al. (2006) observed 1-3 m of displacements of the exposed faults along the SW-NE escarpment. They displaced the upper part of the Middle Member (~35kyr) and perhaps younger Lisan deposits. Bartov (1999), Al-Zoubi and ten-Brink (2001) related the western fault boundary (Figure 4, from 729-3459 to 737-3472) to the ongoing salt tectonics underneath the Lisan wave-cut platform (Figure 3).

On Figure 2, the topographic contour lines -395m and -422m corresponding respectively to the shoreline in 1963 and in 2009 have been drawn. They underline that during the last fifty years, the Dead Sea level had decreased. From 1977, the Lisan peninsula became a land bridge between the eastern and the western coasts because of the drying up of the Lynch Strait. The Dead Sea split in two parts. The salt remains soak the recently emerged lands.

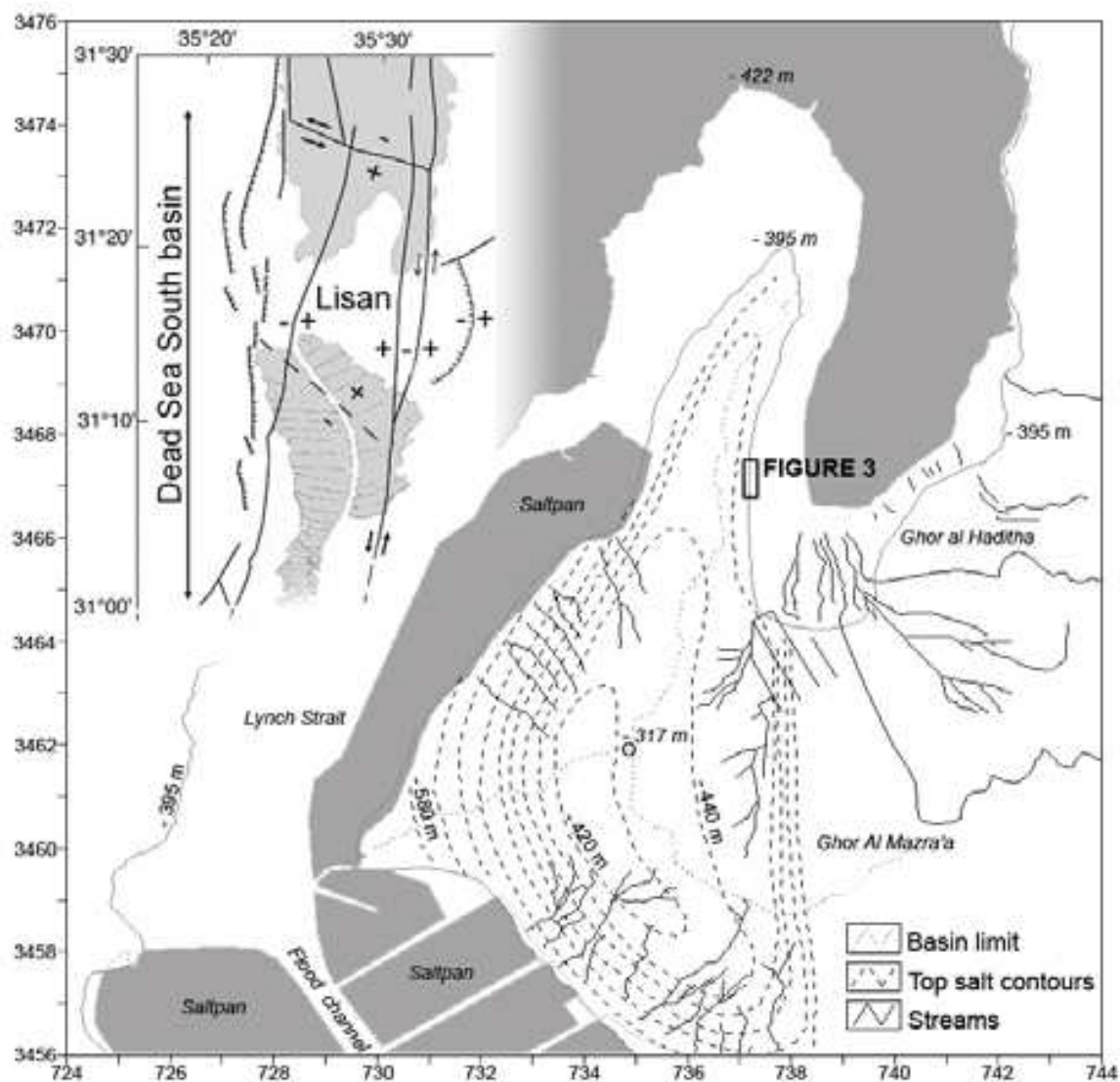


Fig. 2. Top salt of the Lisan diapir (contours from “The salt upwarp of El Lisan”, map compiled by Bender, 1967, and Abu-Ajamieh, 1987). The radial network of ephemeral streams emphasizes the location of maximum thrust (see elevation point -317m, top of the Lisan). Upper right inset displays the major faulted zones and discontinuities as well as the upthrown and downthrown fault blocks in the Dead Sea southern basin (based on Ben Avraham 1997, Ben Avraham and Lazar, 2006). Coordinate are expressed in UTM km, 36, WGS84.

They are thus susceptible for dissolution and compaction. The Lisan tectonic block (Figure 2, inset) gathers the highest concentration of sinkholes and subsidence in the whole Dead Sea area (Closson et al., 2009a). Along the eastern side, Sunna (1986) and Bartov et al. (2006) have interpreted the fault network (Figure 4, from 737-3456 to 737-3470), as one of the strike-slip faults that bound the Dead Sea pull-apart structure. Sub-parallel normal faults trending N-S have formed a 50 m stepped escarpment toward the flat Ghor Al Haditha – Mazra’a graben. This fault zone displaces post-Lisan (<15kyr) deposits. Its northern part is manifested by normal faults dipping to the east (Figure 3), while its southern segment shows smaller displacements with extensive folding.

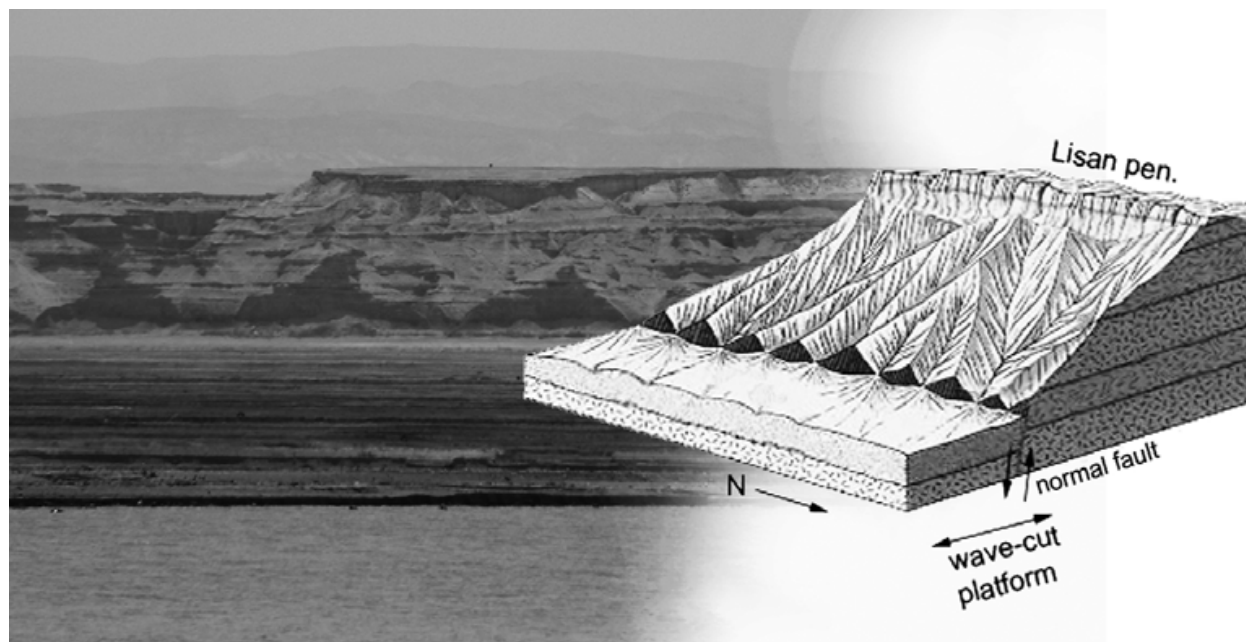


Fig. 3. Vestiges of a fault plane preserved in an alignment of triangular facets. The fault scarp had been produced by active normal faulting along the eastern margin of the former Lisan peninsula. Repeated faulting has produced a rock cliff tens of meters high. Erosion modified the fault scarp but, because the fault plane extends hundreds of meters down into the bedrock, its effects on erosional landforms persisted for several thousand years.

Folds in the Lisan formation delineate the structures of some sub-domes (e.g. Figure 4, lineaments at 734-3460 and at 736-3457) and indicate that it is still rising. Sunna (1986) and Bartov et al. (2006) studied the overall peninsula at the exception of the emerged lands (between the elevations of -395 m and -422 m, see Figure 4). This surface had been investigated more recently, mainly by using remote sensing techniques (Closson, 2005a, 2005b; Closson et al., 2007). Figure 4 shows a major elongated dome with smaller sub-domes located at its southern edge. The structural high of the center of the main dome is located at coordinates 735-3462 (Figure 4, lineaments). Localized joints radiating from this center are found in many places. They are the consequences of the flexure of the dome structure. In the vicinity, the folds have a wavelength of 50-100 m and their amplitude is 10-20 m (734-3462). The folding postdates the base of Upper Member of the Lisan formation. (~32 kyr) and was active during the deposition of the Upper Member (32-15 kyr) due to thickness variation near the folds (Bartov et al., 2006). Southward, the major southern dome (Figure 4, lineaments at 736-3458) has a structural peak of -323 m, it is about 3 km long and 2 km wide with an axis orienting at N45E. The dome is flanked by minor folds dipping 3°- 10° with a wavelength of about 100 m. A few hundred meters southeastward, another dome has a peak of -340 m (Figure 4, faults at 738-3457). It is 3 km long and 1.5 km wide with an axis oriented at N30E. It is characterized by secondary folds crossing the structure and trending 90E-100E with flank dipping up to 40°.

A depression separates these two very different structural domains and supports the location of a major fault zone in between. In this area one fault expose strikes N23E and displaced the top of the Lisan formation (738-3458).

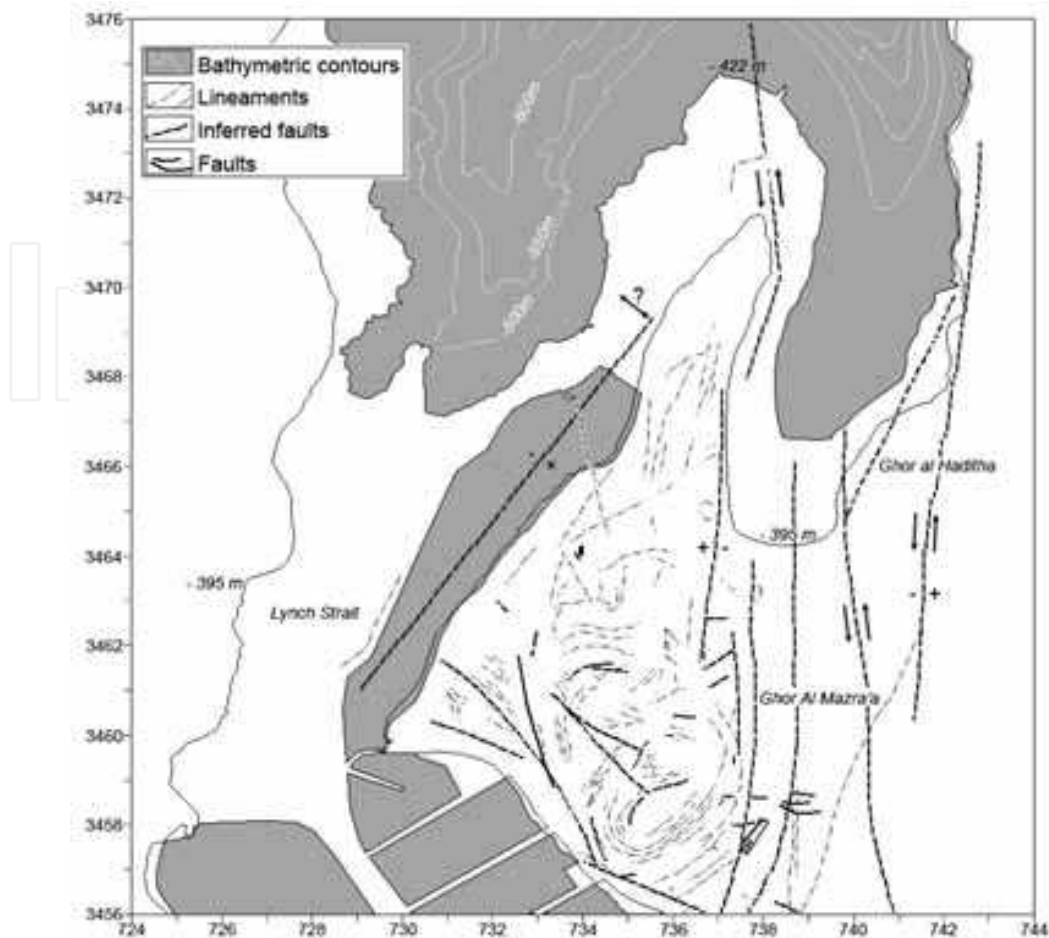


Fig. 4. Lineaments and (inferred) faults of the Lisan, Mazra'a and Ghor Al Haditha area, Jordan, based on the work done by Sunna, 1986; Closson et al., 2003a; Closson et al., 2003b; Closson et al., 2005; Closson, 2005a, b; Diabat, 2005; Bartov et al., 2006; Closson et al., 2007; Closson & Abou karaki, 2009a, b; Closson et al., 2010a, b; Bathymetric contours (Hall, 1997) allow identification of deep and wide submarine canyons that could result from the erosion contemporary to a near complete drying up of the Dead Sea (Neev and Emery, 1967). Topographic contour lines of -395m and -422m correspond respectively to the shoreline in 1963 and in 2009.

## 2.2 Current rates of deformation

When dealing with ground displacements in the Lisan area, six major constraints have to be taken into account:

- the horizontal strike slip movement of the JDST;
- the subsidence of the pull-apart basin;
- the rising of the salt diapir;
- the compaction of the sediments in the zones that have emerged during the last 50 years;
- the possible (but never detected) isostatic rebound in the same zone in relation with the rapid disappearance of about 28 m of Dead Sea brine (-395m in the mid-1960s to -423m in 2010) (E. Salameh, personal communication);
- the dynamic of the halokarst in relation with the Dead Sea level lowering.

The first four are briefly summarized below. The fifth is hypothetical and had not yet been taken into consideration. The latest point had been tackled in Closson et al. (2007).

### **2.2.1 The horizontal strike-slip movement of the JDST and the subsidence of the pull-apart basin**

The modern slip rate is still under debate. Geological observations, however (mostly south of 33°N) suggest nearly pure left-lateral strike-slip faulting and estimated slip rates range between 1 and 20 mm/yr with preferred values around 5 to 7 mm/yr (Freund et al., 1968; Garfunkel et al., 1981; Gardosh et al., 1990; Ginat et al., 1998; Klinger et al., 2000; Niemi et al., 2001; Pe'eri et al., 2002; Ferry et al., 2007). The central part of the JDST is an active fault zone. The historical and instrumental seismicity data suggest that it has generated magnitude 7 (magnitude equivalent) or even larger earthquakes, approximately once every few hundred years. In the XX century, three well documented instrumental earthquakes  $5 < M < 6$  occurred in or very close to the Dead Sea proper in 1956, 1979 (Figure 1, focal mechanism), and 2004 (Abou Karaki, 1987). The distribution of late Pleistocene subsidence in the central Dead Sea Basin is controlled by the local tectonic regime. The normal border faults show a maximum subsidence rate of 0.3 mm/yr of the rim or median block. This block extends basinward up to about 2.5 km where an oblique fault related to the strike-slip segment causes a 0.6 mm/yr subsidence (Bartov and Sagy, 2004).

### **2.2.2 Lisan diapir uplift and subsidence**

Bartov et al. (2006) postulated a long-term uplift rate of 2 mm/yr, based on the depth of the Pliocene salt (>3500 m). The Holocene dome structure indicates ongoing deformation. The center and margins of the dome are undergoing different geomorphologic process. Channels deeply incised the margins but no significant incision is found in the central area.

The upper member of the Lisan Formation is truncated due a transgressive episode of the lake during the Holocene. It occurred ~6000 years B.P. and reached of -370 m. Bartov et al. (2004) deduced that the dome raised and passed over the elevation of -370 m. Taking the present datum of the truncated top of the structure (-315 m) as a marker, the dome was raised 55 m during the last ~6000 years. This indicates an average uplift rate of 9 mm/yr.

From interferometric processing applied to 16 ERS scenes with the JPL Sar processor, Baer et al. (2002) observed that "change interferograms show no sign of uplift in the southern or central domes where the diapir is closest to the surface. Possible evidence for uplift is seen in the northern part of the peninsula. Here, 10 mm and 20 mm of uplift are observed in the 22- and 50-month interferograms, respectively, suggesting an average uplift rate of 4–5 mm/yr". However, Shimoni et al. (2002) published a cumulated 93 months vertical deformation map from different profiles (11-Jun-92 to 21-Mar-99) where two uplift areas characterized by a maximum of 30 mm (4 mm/yr) had been delineated. Subsidence zones were also located north and south of the Lisan with value of 150 mm (22 mm/yr). Here, the DORIS software was used to process a dataset of 17 ERS scenes.

## **3. Material and methods**

### **3.1 Satellite images and software**

Radar interferometric techniques have been applied to 27 scenes (single look complex format) acquired by three different sensors onboard satellites: 14 ERS AMI-SAR (8 descending; 6 ascending), 2 ENVISAT ASAR, and 11 ALOS PALSAR (4 descending; 7

ascending). Two interferometric processors have been used to perform the study: Sarscape module (version 4.2) of Envi and Radar Mapping Suite (version 2010) of Erdas Imagine. Table 1 lists the images based on the date of acquisition.

ERS	ERS	Envisat	Alos	Alos
ASC	DSC	DSC	ASC	DSC
29-May-99	10-Dec-00	27-Apr-08	20-Dec-08	17-May-08
11-Oct-97	4-Jul-99	23-Mar-08	4-Nov-08	1-Apr-08
10-Oct-97	11-Oct-97		4-May-08	15-Feb-08
16-Dec-95	14-Jul-96		19-Mar-08	15-Nov-07
15-Dec-95	29-Jul-95		2-Feb-08	
30-Jun-93	30-Jul-95		18-Dec-07	
	5-Aug-93		2-Nov-07	
	11-Jun-92			

Table 1. Image dataset

3.2 Radar interfrometry techniques

Radar interfrometry techniques exploit the phase information of the signal emitted and received by a sensor onboard a satellite to generate digital surface models (Interferometric Synthetic Aperture Radar or InSAR technique) and/or ground motion images (Differential InSAR or DInSAR technique). These techniques have been successfully used for years to study the topsoil deformations in the Dead Sea area (e.g. Derauw 1999, Baer et al. 2002, Shimoni et al. 2002, Closson et al., 2003, closson et al., 2010). However, practically all published results were obtained from the processing of ERS-1 and ERS-2 satellite data. In this work we exploit the images acquired from the following sensors: ERS AMI-SAR, ENVISAT ASAR (both characterized by C-band, wavelength = 5.6 cm), and ALOS PALSAR which uses L-band (wavelength = 23.62 cm). Table 2 brings an overview of the sensors and their satellites.

The principle of the InSAR and DInSAR techniques is briefly summarized. Two images acquired from the same orbit but at different time (46 days apart for ALOS and 35 days for ERS and ENVISAT - Table 2), and with a similar incidence angle are necessary to generate an interferogram (image of the phase difference).

As an example, Figure 5 displays the principle of InSAR for digital surface model generation. In  $T_0$ , a radar antenna onboard a satellite acquires one image of a point P at the ground surface. The measure of the distance MP leads to the phase  $\Phi_M$ . In  $T_1$ , the same or a twin satellite passes over the area of interest but not exactly at the same position. The measure of the distance SP leads to the phase  $\Phi_S$ .

The InSAR techniques exploit the phase difference ( $\Delta\Phi_{INT} = \Phi_S - \Phi_M$ ) which is related to the distance (SP - MP). Considering a single pixel footprint:

In  $T_0$ :  $\Phi_M = 2 * MP * (2\pi / \lambda) + \Phi_0$

In  $T_1$ :  $\Phi_S = 2 * SP * (2\pi / \lambda) + \Phi_0$

InSAR equation:  $\Delta\Phi_{INT} = \Phi_S - \Phi_M = (SP - MP) * (4\pi / \lambda)$

$\lambda$  = radar wavelength (5.6 cm for ERS and ENVISAT, 23.6 cm for ALOS)

	ERS (C band)	ENVISAT (C band)	ALOS (L band)
Altitude of the satellite	~790 km	~790 km	~700 km
Central frequency band	5.3 GHz	5.331 GHz	1.27 GHz
Wavelength	5.6 cm	5.6 cm	23.6 cm
Polarization	VV	VV HH HH/HV VV/VH HH/VV	VV HH HH/HV VV/VH
Incidence angle	~23.2°	15° - 45°	~38.7°
Maximum perpendicular baseline	1100 m	1100 m	15380 m
Resolution (range)	~24.5 m	30 - 150 m	~8.6 m
Resolution (azimuth)	~5 m	~5 m	~5 m
Swath	~100 km	58 - 110 km	~70 km
Repeat cycle	35 days	35 days	46 days
phase noise (*)	2.1 mm	2.1 mm	3.3 mm
(*) i.e., line of sight (LOS) precision of over the 100 m to 5000 m wavelength band			
fringe rate	4	4	1
Coherence	less	less	better
Tropospheric effects	Identical	Identical	Identical
Ionospheric effects	better	better	~17 times greater than C-band
Phase gradients/Greater deformation	less	less	better
Measurement accuracy	better	better	Less (~1.6 times)

Table 2. List of some parameters allowing a comparison between sensors used in this work.

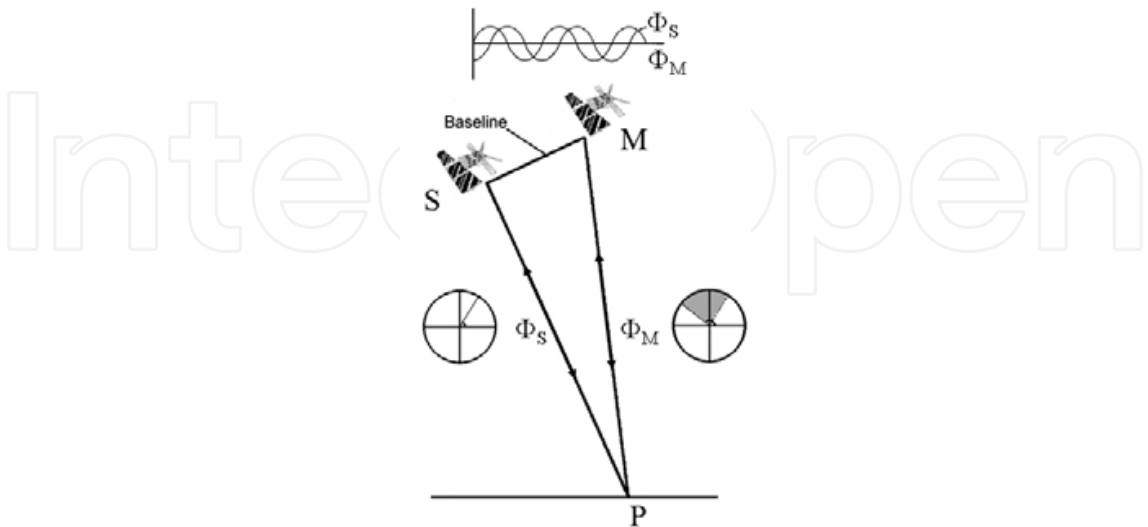


Fig. 5. Principle of InSAR for digital surface model generation. M = “Master” or reference image acquired in  $T_0$ . S = “Slave” images acquired in  $T_0 + \Delta T$  ( $\Delta T = 1$  day (ERS),  $n \cdot 35$  days (ERS, ENVISAT),  $n \cdot 46$  days (ALOS))

Among others,  $\Delta\Phi_{INT}$  gathers information about the topography (“topographic fringes”). An analogy can be done between the “fringes” that appear over an interferogram and the surface between two contours of a topographic map. In the same way, the “altitude of ambiguity” of an interferogram is similar to the contour interval.

The sensitivity to the topography of an interferogram (“altitude of ambiguity”) depends on the relative position of the two sensors (distance MS). Among others, it depends on the “perpendicular” baseline parameter. The value of the “altitude of ambiguity” increases drastically when the distance of the perpendicular baseline tends to zero. An interferogram generated from two acquisitions having a very short perpendicular baseline will present only a few “topographic fringes”. In other words, a short perpendicular baseline means an interferogram equivalent to a topographic map with a few contours and a large contour interval. Therefore, if a concentration of fringes is observed over such an interferogram, then ground displacements are suspected.

Conversely, when the perpendicular baseline increases, the “altitude of ambiguity” decreases so that the interferogram will reveal the most subtle topographic variations of the ground surface. A limitation exists for the length of the “perpendicular baseline”. Indeed, the more the perpendicular baseline increases, the more the image of point P (Figure 5) will differ so that it become impossible to coregistrate the two acquisitions and compute the phase difference. Table 2 gives the maximum perpendicular baseline allowed (in theory).

The more the temporal baseline increases, the more the possibility of ground movements increases. Surface displacements happen for various reasons (e.g. water or oil extraction lead to subsidence while volcanoes inflation leads to uplift). In this case,  $\Delta\Phi_{INT}$  gathers information about the topography and ground movements (“displacement fringes”) that have occurred between the two acquisitions. Figure 6 displays the principle of DInSAR for deformation measurement: a subsidence occurred between the two acquisitions and the point P dropped to the position P’.

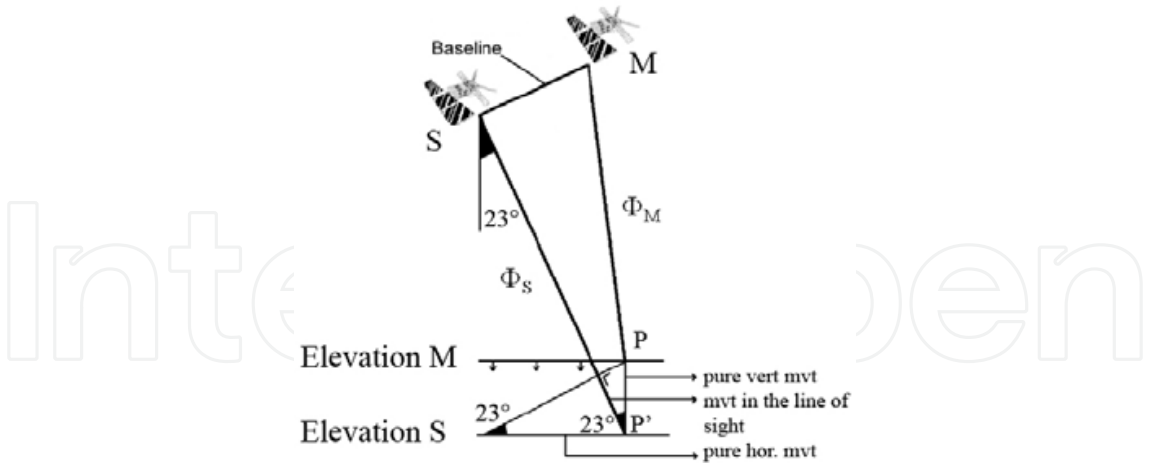


Fig. 6. Principle of DInSAR for deformation measurement. As an example, 23° is the incidence angle for ERS satellites.

In  $T_0$  :

$$\Phi_M = 2 * MP * (2\pi / \lambda) + \Phi_0$$

In  $T_1$  :

$$\Phi_S = 2 * SP' * (2\pi / \lambda) + \Phi_0$$

DInSAR equation:

$$\Delta\Phi_{INT} = \Phi_S - \Phi_M = (SP - MP) * (4\pi / \lambda) + (SP' - SP) * (4\pi / \lambda)$$
$$\Delta\Phi_{INT} = \Delta\Phi_{Topo} + \Delta\Phi_{Mov}$$

If one focuses only on the ground movements ( $\Delta\Phi_{\text{Mov}}$ ), the “topographic fringes” have to be retrieved using the technique of “differential interferometry”. By simulating  $\Delta\Phi_{\text{Topo}}$  from an available digital elevation model of the area of interest, it is possible to obtain  $\Delta\Phi_{\text{Mov}} = \Delta\Phi_{\text{INT}} - \Delta\Phi_{\text{Topo\_simulated}}$

From the DInSAR equation one can deduce that  $\Delta\Phi_{\text{Topo}} = (SP - MP) * (4\pi / \lambda)$  is a function of the distance between M and S while  $\Delta\Phi_{\text{Mov}} = (SP' - SP) * (4\pi / \lambda)$  is independent of the baseline.  $\Delta\Phi_{\text{INT}}$  is therefore more sensitive to the ground displacement than the topography. From Figure 6, one can deduce that  $\Delta\Phi_{\text{Mov\_pure vertical}} = (\Delta\Phi_{\text{Mov}} / \cos 23^\circ) * (\lambda / 4\pi)$ . One centimeter of ground displacement along the line of sight will lead to  $\Delta\Phi_{\text{Mov}} \sim 127^\circ$ . Considering a typical noise of an interferometric phase of the order of  $\pi/6 = 30^\circ$ , movements of about 2.5 mm can be detected. With respect to the topography, if a difference of elevation of 20 m is considered, then the  $\Delta\Phi_{\text{Topo}}$  will be about  $43^\circ$  with a baseline of 50 m and about  $8.6^\circ$  for a baseline of 10 m (in the case of ERS satellite).

Table 3 shows an example of the spatial and temporal baselines available for a set of 6 ERS acquisitions in ascending mode. Each image is chosen as the reference and spatial and temporal characteristics of the other scenes calculated respectively.

Spatial						
	29-May-99	11-Oct-97	10-Oct-97	16-Dec-95	15-Dec-95	30-Jun-93
29-May-99		75	294	81	253	86
11-Oct-97			369	156	178	151
10-Oct-97				213	547	218
16-Dec-95					334	5
15-Dec-95						339
30-Jun-93						

Temporal						
	29-May-99	11-Oct-97	10-Oct-97	16-Dec-95	15-Dec-95	30-Jun-93
29-May-99		595	596	1260	1261	2159
11-Oct-97			1	665	666	1564
10-Oct-97				664	665	1563
16-Dec-95					1	899
15-Dec-95						898
30-Jun-93						

Table 3. Spatial and temporal baselines of 6 ERS images acquired in ascending mode. Grey cells are discussed in the text.

The pairs 10/11-Oct-97 and 15/16-Dec-95 have been acquired at one day apart, when the ERS 1 and 2 satellites were orbiting together. Because of this short delay, the scatters on the ground are generally not disturbed (no displacement such as displayed on Figure 5) and thus allow an accurate measurement. The baselines are wide (369 m and 334 m) allowing a detailed description of the topography. One pair is characterized by a very short baseline:

30-Jun-93 and 16-Dec-95 = 5 m. In this case, the interferogram displays essentially ground displacements over a period of 899 days (if they exist).

## 4. Results

### 4.1 Digital surface model of the Lisan and features extraction

Figure 7 displays a digital surface model realized by applying InSAR techniques to a “tandem” pair of ERS images acquired in ascending mode 15/16-Dec-95. The perpendicular baseline is quite high with 334 m leading to an “altitude of ambiguity” of 31.5 m. No atmospheric artifact has been found on this pair (Derauw 1999).

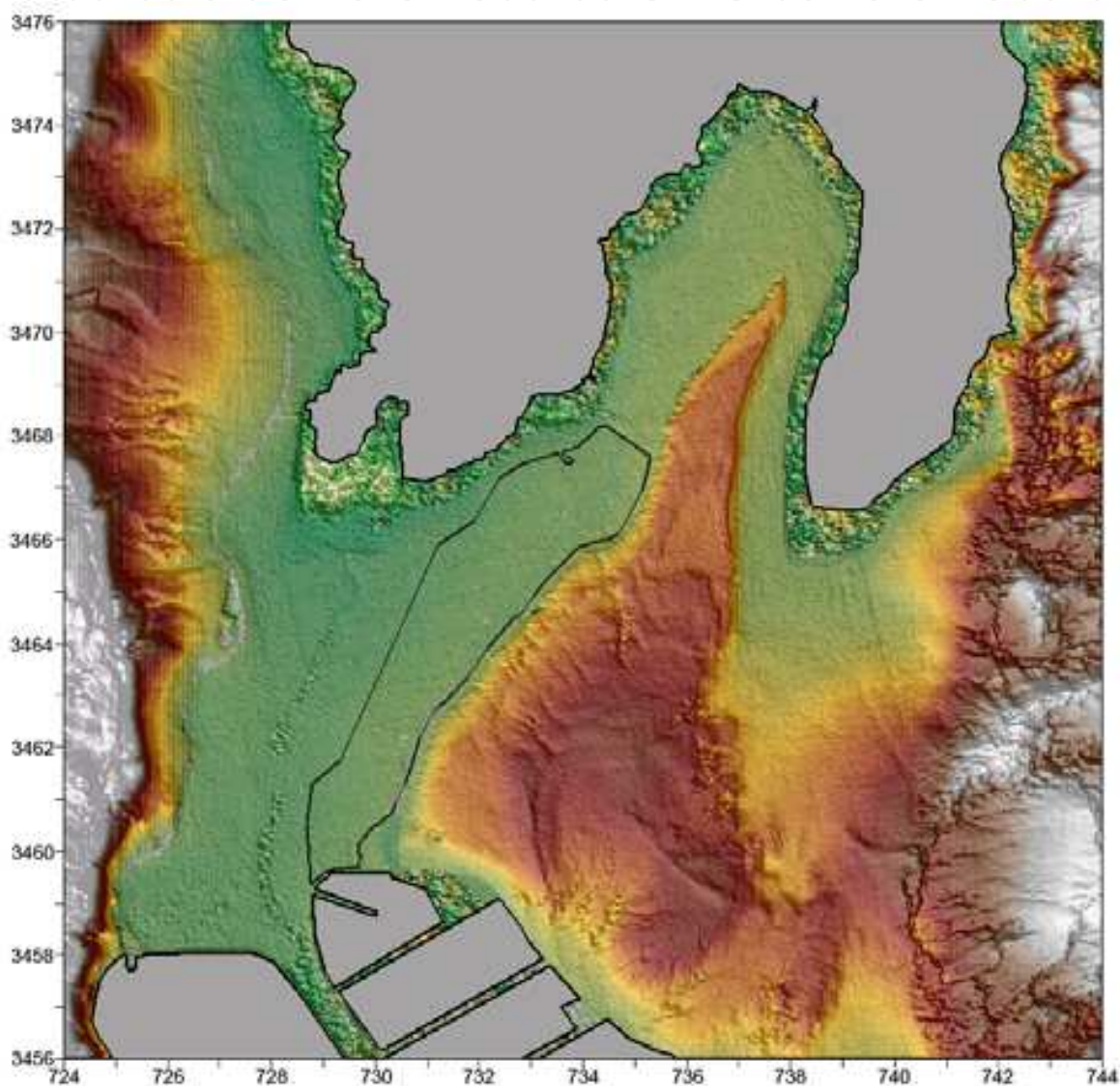


Fig. 7. Geocoded digital surface model of the Lisan area based on the “tandem” pair of ERS images acquired in ascending mode, period: 15-Dec-95 to 16-Dec-95; perpendicular baseline: 334 m; temporal baseline 1 day.

Water surfaces have been masked with data deriving from an acquisition of 2009. As the Dead Sea level is dropping at a rate of about 1 m/yr, the mask does not fit exactly with the water surface of December 1995. The disturbed zone along the shore corresponds to the

surface that appeared between 1995 and 2009. West of the Lisan, the external limit of a major saltpan is represented by a black line.

Spatial Analyst tools dedicated to surface and hydrological available in ESRI ArcGIS have been used to extract features such as contours, curvature, slopes, orientations, drainage pattern, watersheds... They allowed a better description and understanding of the geomorphology. The model presented on Figure 7 shows 4 different zones:

- A relatively high land area corresponding to the former peninsula which is an undulated to flat plain with isolated hills (dark to light brown – coord. 734-3462);
- The badlands characterized by steep slopes and deep canyons occurs mainly in the southern part and along the periphery of the high land zone (yellow – 734-3459);
- The low lands occupy the eastern part of the Lisan (yellow-light green – 738-3464);
- The wave-cut platform surrounding the former peninsula in the west, north and northeastern sides (green – 734-3466).

The regional drainage pattern is radial, locally it can be dendritic or parallel such as in the southern and western parts. In all cases the talwegs network reflects the local weakness zones related either to the salt rising or the strike-slip fault displacement. Visual extraction of linear features had been carried out by using a large panel of color palettes emphasizing specific topographic contrasts.

The accuracy of the digital surface model is given by the image of the interferometric phase coherence (measure the similarity between the two scenes backscattering) associated with the curve of the theoretical standard deviations of the elevations. Figure 8 presents a standard deviation map based on the coherence image. A quarter of the full scene is represented. Because the estimator of the standard deviations is only valid for the higher coherence values, the computation had been done for the coherence values upper than 0.5. The histogram of the standard deviations shows that the theoretical average accuracy over the scene is about one meter.

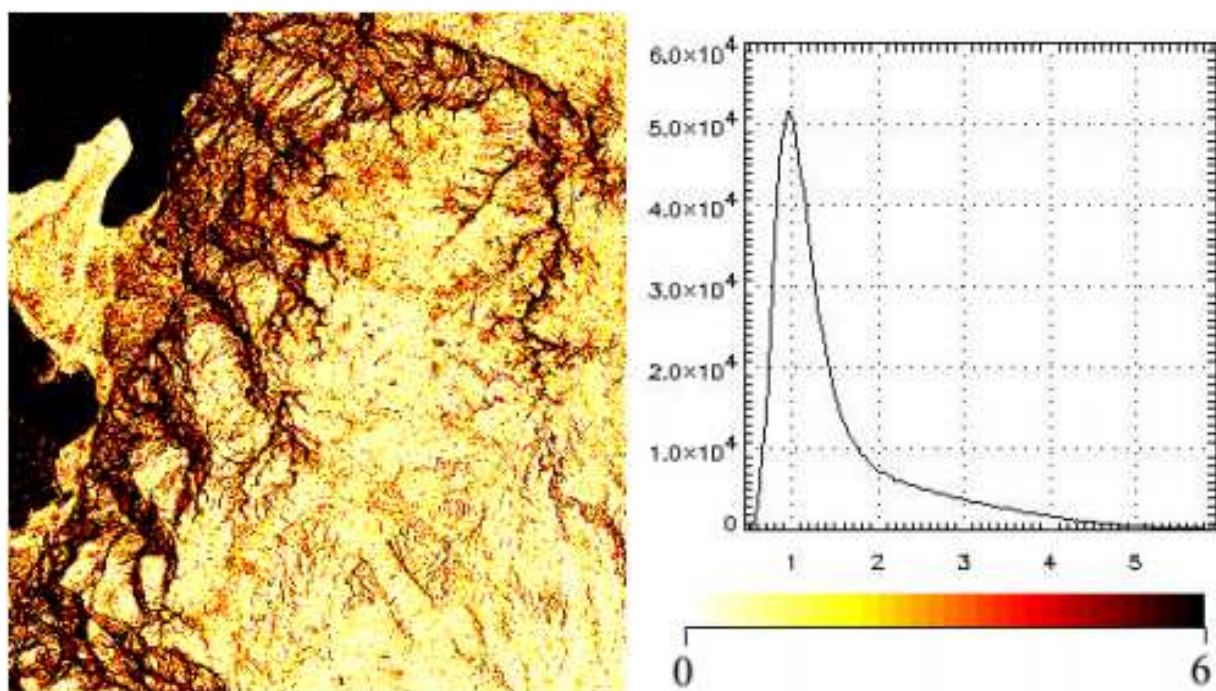


Fig. 8. Standard deviation map based on the coherence image (Derauw, 1999; Closson 2005b).

4.2 Ground displacements

It is impossible to present the whole interferograms that have been computed in this research. As an example, Table 3 shows 15 possible combinations but only 10 are able to bring valuable information. Indeed, four cases lead to a total decorrelation in the interferogram. They are the combinations characterized by the spatial baseline of 547 m and the temporal baseline of 2159, 1564 and 1563 days. Among the whole combinations of the dataset presented in Table 2, a selection of four relevant unwrapped and geocoded interferogram is presented (Figures 9-12). Each case presented in Table 4 emphasizes a particular relation between the spatial- temporal baseline and the type of sensors.

			Spatial - Temporal baselines			
			Small - Short	Small - Wide	Large - Short	Large - Wide
ERS	C-band	Asc				Figure 12
ENVISAT		Dsc		Figure 10		
		Asc				
		Dsc			Figure 11	
ALOS	L-band	Asc	Figure 9			
		Dsc				

Table 4. Characteristics of the various interferograms that can be generated from the available dataset. This table is helpful when comparing results.

4.2.1 Deformation fields with small spatial baseline and short temporal baseline – ALOS data

Figure 9 shows an interferogram computed from two ALOS Palsar scenes acquired the 02-Feb-08 and the 19-Mar-08, i.e. 46 days apart. The normal baseline is 110 m leading to an altitude of ambiguity of 582 m. The Lisan peninsula is only covered by 1/6 of topographic fringe. The wavelength is 23.6 cm (L-band), therefore one fringe cycle will represent a displacement in the line of sight of 118 mm, about four times more than in the case of ERS.

A total decorrelation (dark purple color) occurred over the high land area (e.g. from 734-3460 to 737-3466) and over the farming zones east of the peninsula (from 739-3461 to 741-3466). The decorrelation over the high land is caused by the very low backscattering of the surface. The smooth (relatively to the wavelength) surface acts as specular reflectors and do not reflect much signal back to the radar.

By comparison with Figure 11, practically no decorrelation occurred in the Lynch Strait, at the exception of the surfaces covered by water (727-3457).

Strong subsidences are found in:

- 728/729-3460/3461, very close to the dike of the major saltpan occupying the western wave-cut platform of the Lisan;
- 730-3468, the delta of wadi Araba which is always aggrading due to the lake level lowering;
- and e.g. in 739-3470, the recently emerged shoreline constitute a ribbon of subsidence buffering the northern Lisan.

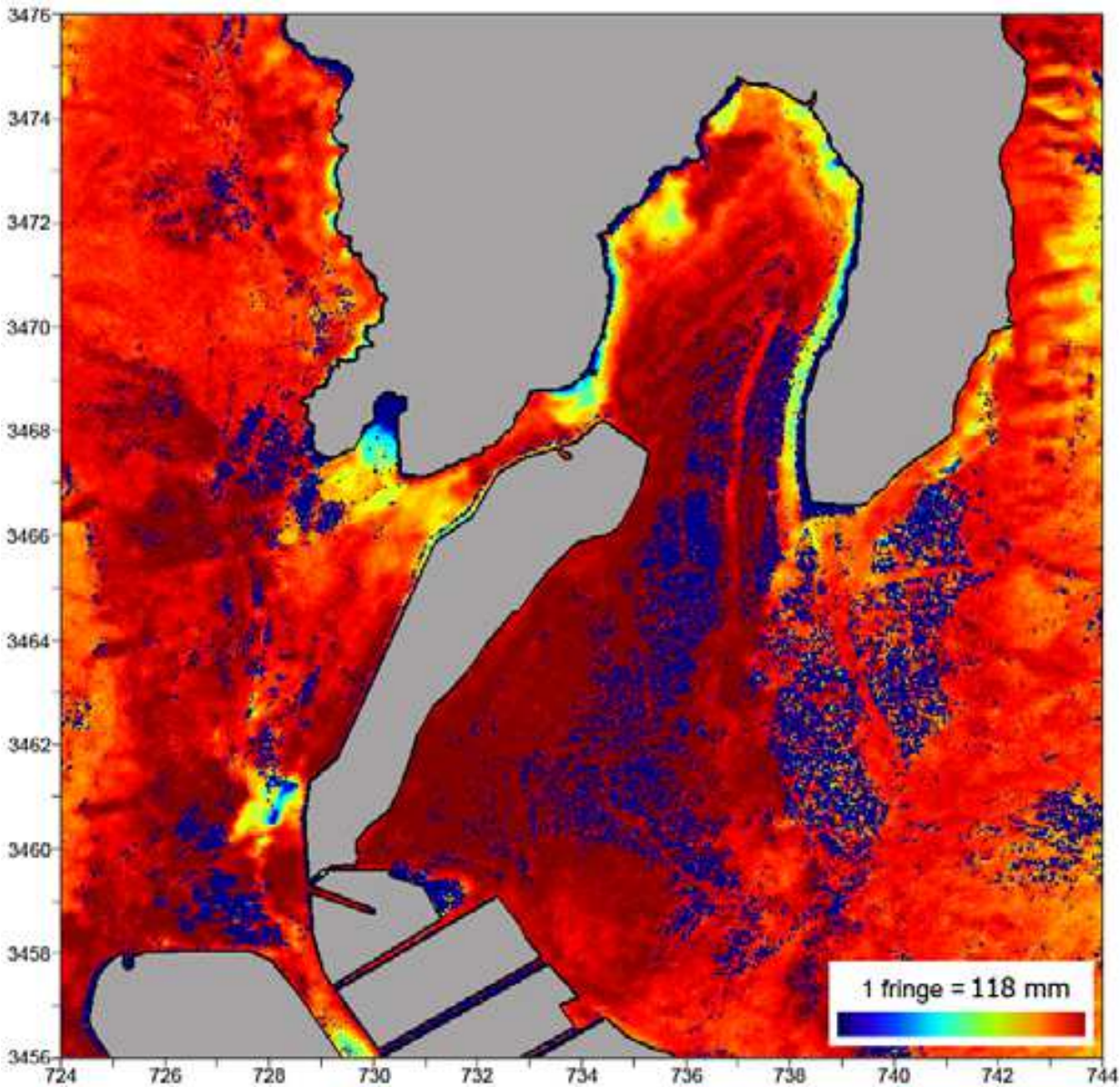


Fig. 9. Geocoded interferogram of an ALOS images pair, ascending mode, period: 02-Feb-08 to 19-Mar-08. Perpendicular baseline: 110 m; temporal baseline 46 days.

**4.2.2 Deformation fields with small spatial baseline and wide temporal baseline – ERS data**

Figure 10 shows an unwrapped interferogram of an ERS images pair covering the period 29-Jul-95 to 14-Jul-96. The perpendicular baseline is 13 m and the temporal baseline 350 days. The altitude of ambiguity is 770 m. Taking into account that the maximum elevation over the Lisan is -317 m and the minimum -409 m (in Jul-95: -408.7 m; in Jul-96: -409.6; Arab Potash Company gauge station), the Lisan is only covered by 1/8 of topographic fringe ( $770 \text{ m} / [-317 \text{ m} - -409 \text{ m}]$ ). No atmospheric artifact has been detected by combining the two images with other images of the available dataset (Table 1). The cycle of spectrum color palette corresponding to one fringe indicate that surface displacements occurred all over the peninsula (see Figure 13 for details) during the period of observation. Each cycle represents

a ground displacement in the line of sight with amplitude of 28 mm, i.e. half of the ERS-AMI sensor wavelength. The main zones of interest are located below:

- 735-3466, 736-3468, 736-3469, and 737-3470, four uplift areas have affected the northern part of the Lisan;
- 737-3472, 738-3472, 736-3461, 737-346, 735.5-3459, 734.5-3458, 737-3458 correspond to seven kilometric shallow subsidence areas;
- the noisy surfaces (dark blue), mainly east and west of the peninsula, correspond either to agricultural crops in the graben of Mazra'a - Ghor Al Haditha or to soil moisture, especially in the southern Lynch Strait area. It is also suspected that in several other zones, decorrelation is related to ground displacements whose amplitude is too important to be detected in C-band.

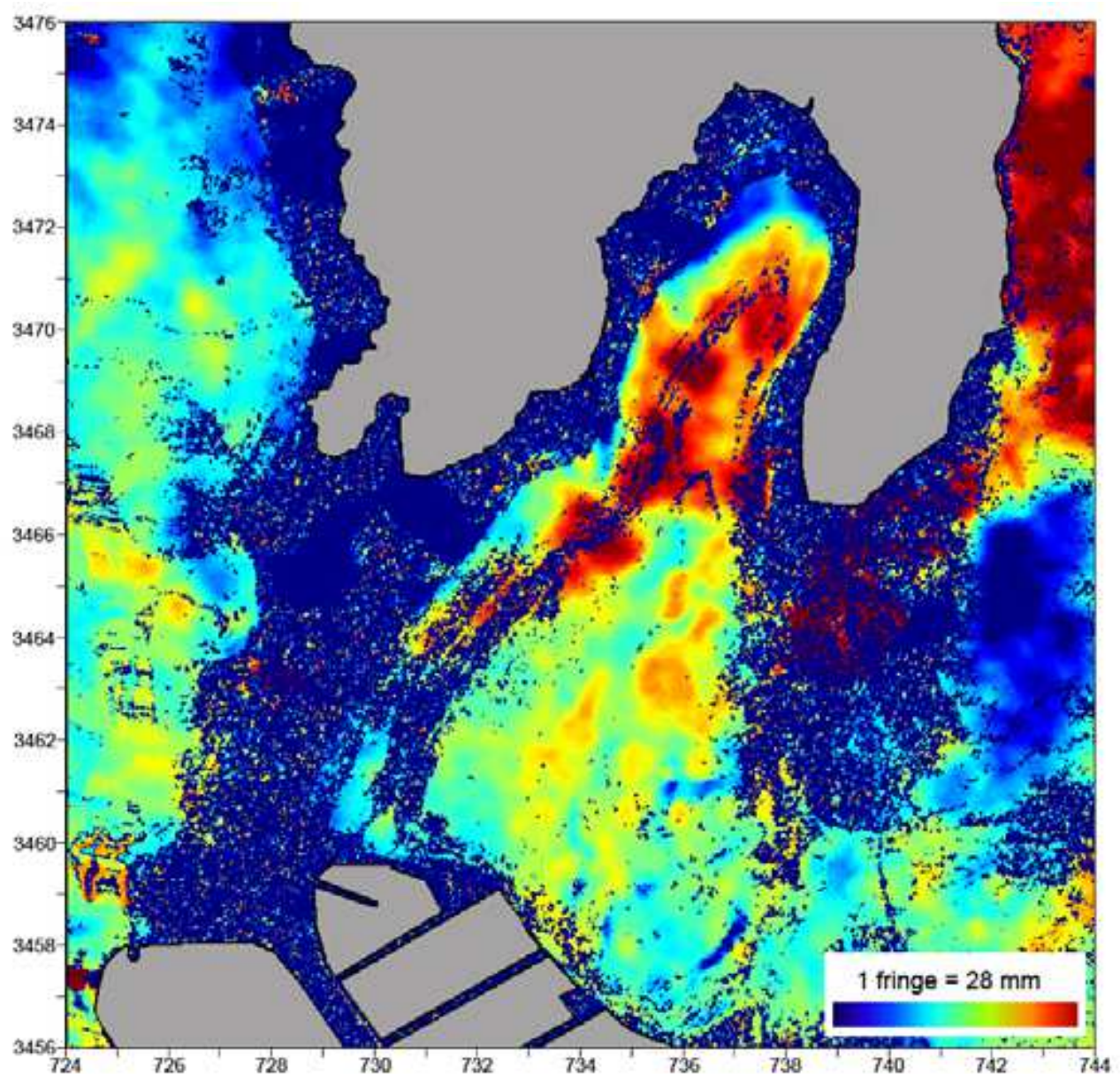


Fig. 10. Geocoded interferogram of an ERS images pair, descending mode, period: 29-Jul-95 to 14-Jul-96. Perpendicular baseline: 13 m; temporal baseline 350 days.

#### 4.2.3 Deformation fields with large spatial baseline and short temporal baseline – ENVISAT data

Figure 11 shows a differential interferogram computed for the period 23-Mar-08 to 27-Apr-08. It extends the period of observation of Figure 9 (02-Feb-08 to 19-Mar-08) but in C-band rather than in L-band. Table 2 indicates that the fringes' rate of Envisat/ERS interferograms are four times greater than the one of ALOS and the general accuracy is 1.6 times less for ALOS too. The normal baseline is 342 m and the altitude of ambiguity 19 m. The topographic phase component had been retrieved from the interferogram with the SRTM data (digital surface model acquired in February 2000). Therefore, the coastal area that appeared between 2000 and 2008 (about 8 m of bathymetric elevation) does not present correct values. As expected, the deformation fields displayed on Figure 11 are in agreement with ones of Figure 9. It is worth noting that the loss of coherence is more important for ALOS than for ENVISAT because of the sensitivity of L-band to the roughness of the ground of the Lisan.

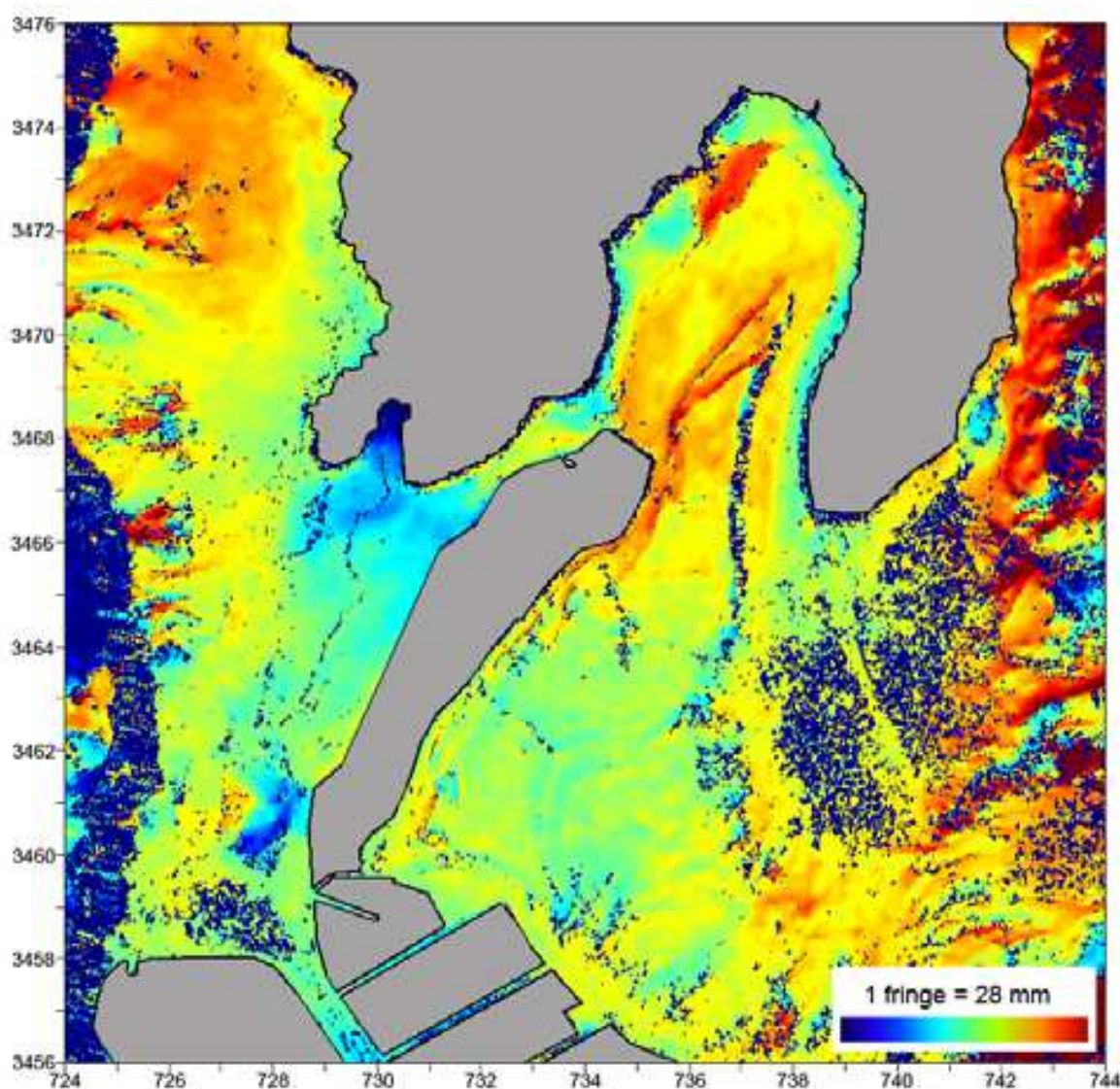


Fig. 11. Geocoded interferogram of an ENVISAT images pair, descending mode, period: 23-Mar-08 to 27-Apr-08. Perpendicular baseline: 342 m; temporal baseline 35 days.

#### 4.2.4 Deformation fields with large spatial baseline and large temporal baseline – ERS data

Figure 12 shows an interferogram spanning over about 3.5 years. The deformations information recorded on Figure 10 are thus included here and fill out with data covering the period not included in Figure 10. The coherence decreased in many places due to the industrial activities over the wave-cut platform. A large part of the northern peninsula had been used as quarries during the period of observation. The zones of interest are located in:

- 732-3460, a large uplift area affected the southwestern part of the Lisan;
- 736/738-3472, kilometric shallow subsidences have affected the northern part of wave-cut platform surrounding the peninsula;
- 736-3461, 734-3459, 737-3458, curvilinear subsidences;

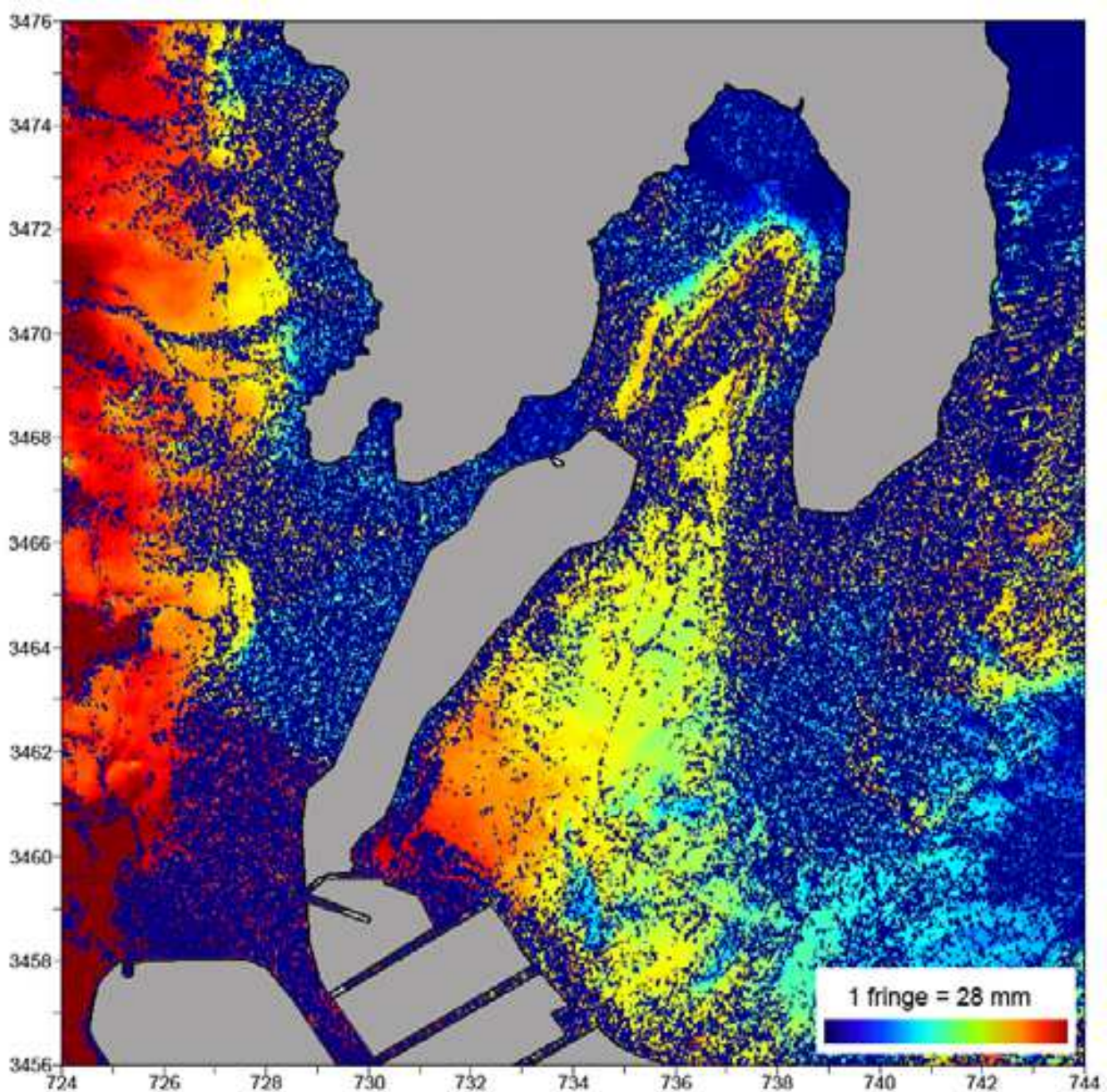


Fig. 12. Geocoded interferogram of an ERS images pair, ascending mode, period: 12-Dec-95 to 29-May-99. Perpendicular baseline: 221 m; temporal baseline 1261 days.

5. Discussion

The knowledge gained from the differential interferogram analysis are the rates of vertical displacements, the location of uplifted and subsidence areas, their spatial extension and evolution through the period of observation. The investigation is done by comparing time series of interferograms and of cross sections such as illustrated in Figure 13. Six cross sections through the interferogram displayed on Figure 10 have been drawn together with their projection over a hillshaded view of the digital surface model displayed in Figure 7.

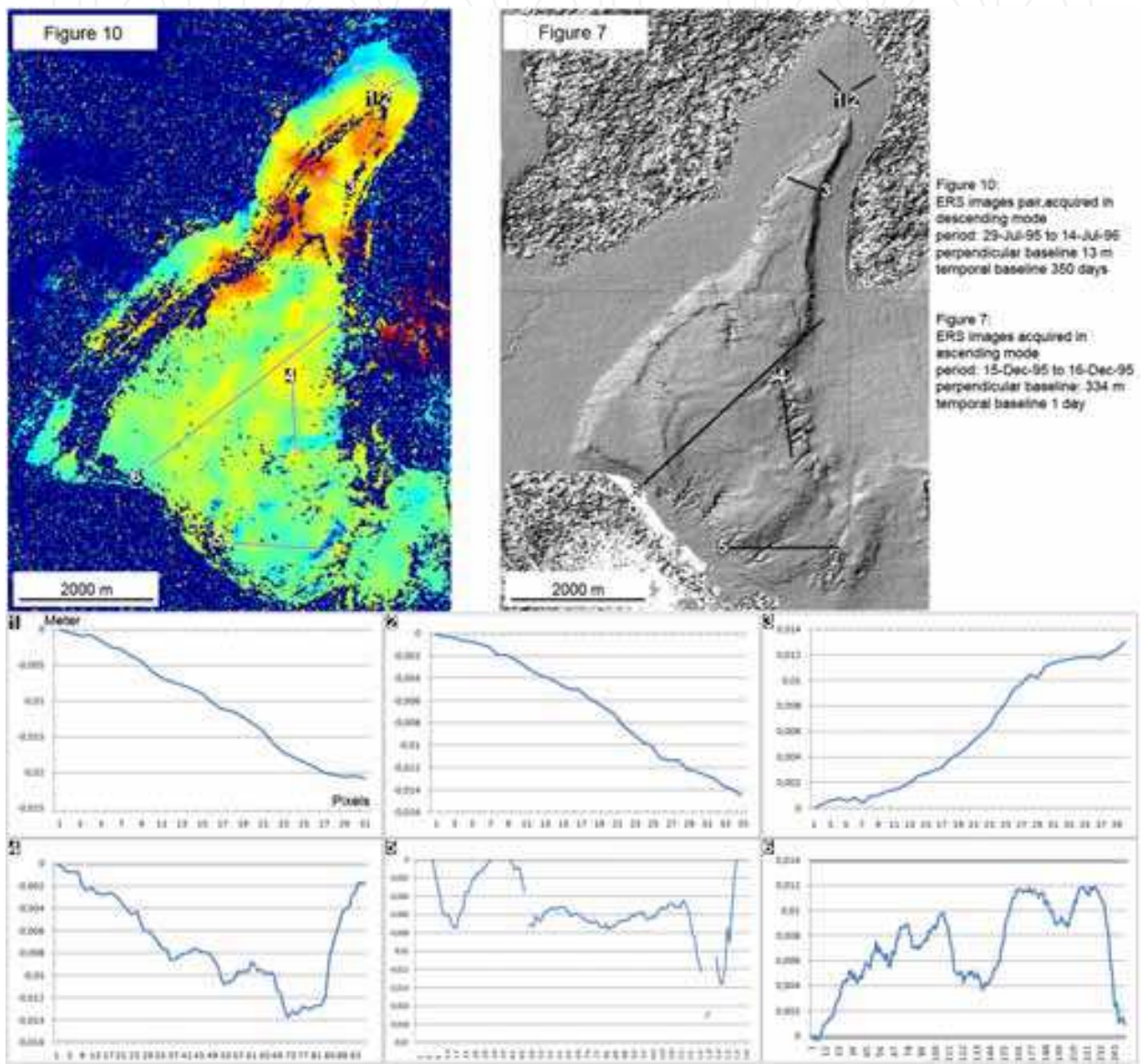


Fig. 13. Evaluation of displacements through cross sections. The ERS Inferferogram is characterized by a perpendicular baseline of 13 m and a temporal baseline of 350 days. The altitude of ambiguity is 770 m and the Lisan is only covered by 1/8 of topographic fringe.

Due to the limited spatial extent of the Lisan area it was not possible to define a reference point far away from the salt diapir which could be considered as a zero phase value for the phase unwrapping process. In consequence, to make comparable the phase variations both in space and time within the Lisan area we have considered arbitrarily the reference sites at

each starting point of the cross sections for which the observed deformation is assumed to be minimal over the studied period.

To avoid this problem, one strategy - not realized in this work - consists to create a reference phase value for each starting point by averaging the unwrapped phase values from the surrounding pixels. This minimal deformation phase value is then used as a common reference for the whole time series of unwrapped interferograms. By this process, the resulting field deformation maps give a relative measure of the ground displacement with respect to this fixed reference point.

### **5.1 Vertical movements affecting the northern Lisan wave cut platform in relation with the Dead Sea level lowering**

The interferograms computed with the image dataset (Table 1) have shown two distinct kilometric areas of subsidence affecting the edge of the northern Lisan wave cut platform. The most extended one is sinking northwestward, the second northeastward (see cross sections 1 and 2, Figure 13). A hectometric sill where ground movements are less important separates them. The location of this sill and of lineaments over the wave cut platform suggested that a major fault N-S oriented crosses this zone (Closson et al., 2003; Closson et al., 2005).

Cross sections 1 and 2 bring knowledge of the vertical movements (X-scale bar is expressed in pixels while Y-scale bar is in meter). The pixel size of the interferogram is 20 meters and the cross sections are nearly similar in length. Cross section 1 indicates that pixel n°31 has been lowered by about 20 mm compared to pixel n°1 between 29-Jul-95 and 14-Jul-96. In the same way, cross section 2 informs that pixel n°35 dropped by 14 mm compared to pixel n°1. Subsidence in area 1 was more active than subsidence zone 2 during this period of 350 days. Other measurements have confirmed that the northern part of the wave-cut platform was in strong subsidence during the 1990s. For example, based on the interferogram displayed on Figure 12, subsidence measurements of 71 mm (area 1) and 70 mm (area 2) were recorded over a period of 1261 days (from 12-Dec-95 to 29-May-99) leading to a rate of 20 mm/year in both areas.

It is worth to be mentioned that during the 1990s, the Arab Potash Company built two major salt evaporation ponds (USD 70M) all along the western Lisan wave cut platform in order to meet its increasing fertilizer production needs. The northernmost unit was destroyed in March 2000 during filling operation. About 1650 m of earthen dike disappeared during the rapid emptying of 55 million cubic meters of Dead Sea brine (Figure 14). The fact is that the place where the dike started to break up is precisely at the location where a maximum of subsidence was recorded (e.g. during the period 29-Jul-95 to 14-Jul-96, see Figure 13 - cross section 1). Fieldwork conducted between 2004 and 2009 in this area have clearly shown that in tens of places the remaining dike is fissuring at an increasing rate. Some flanks of the dikes have also slid, proving the existence of significant ground motions during the present decade since rainfall is a marginal phenomena. In 2010, the southern saltpan still exists. Its external limit had been reproduced on Figure 2 (saltpan, coord. 732-3465). It had been repaired during five years (USD 16M), between 2001 and 2006, and is under continuous surveillance. Fieldwork revealed that sinkholes pierced the earthen dike and the bottom of this saltpan (Closson & Abou Karaki, 2009). In some places, engineers tripled the wide of hectometric dike segments to increase the safety factor... In the area of cross section 2, consolidation and drainage work have been realized at the end of the 1990s until the day of the saltpan destruction. They are still visible in 2010 and attest of the difficulties encountered to stabilize the salt evaporation pond.

Long term and short term measurements carried out with ALOS and ENVISAT data (Table 1) support field observations and above all show a drastic increase in the rate of subsidence by comparison with the rates recorded in the 1990s. For example, Figure 14 presents the result of a cross section in area 1. The rate of subsidence is four times greater than the one observed e.g. by Baer et al. (2002) or by Shimoni et al (2002): 80 mm/year between 18-Dec-2007 to 20-Dec-2008 in place of 20 mm/year between 29-Jul-95 and 14-Jul-96 or between 12-Dec-95 and 29-May-99. By comparison, in area 2, the rate is 25% less than in area 1, i.e. 60 mm/year between 18-Dec-2007 to 20-Dec-2008. In general, the rates of subsidence in area 1 and 2 are quite important but area 1 seems a more active than area 2. This could explain why the dike collapsed in the area 1 in place of area 2.

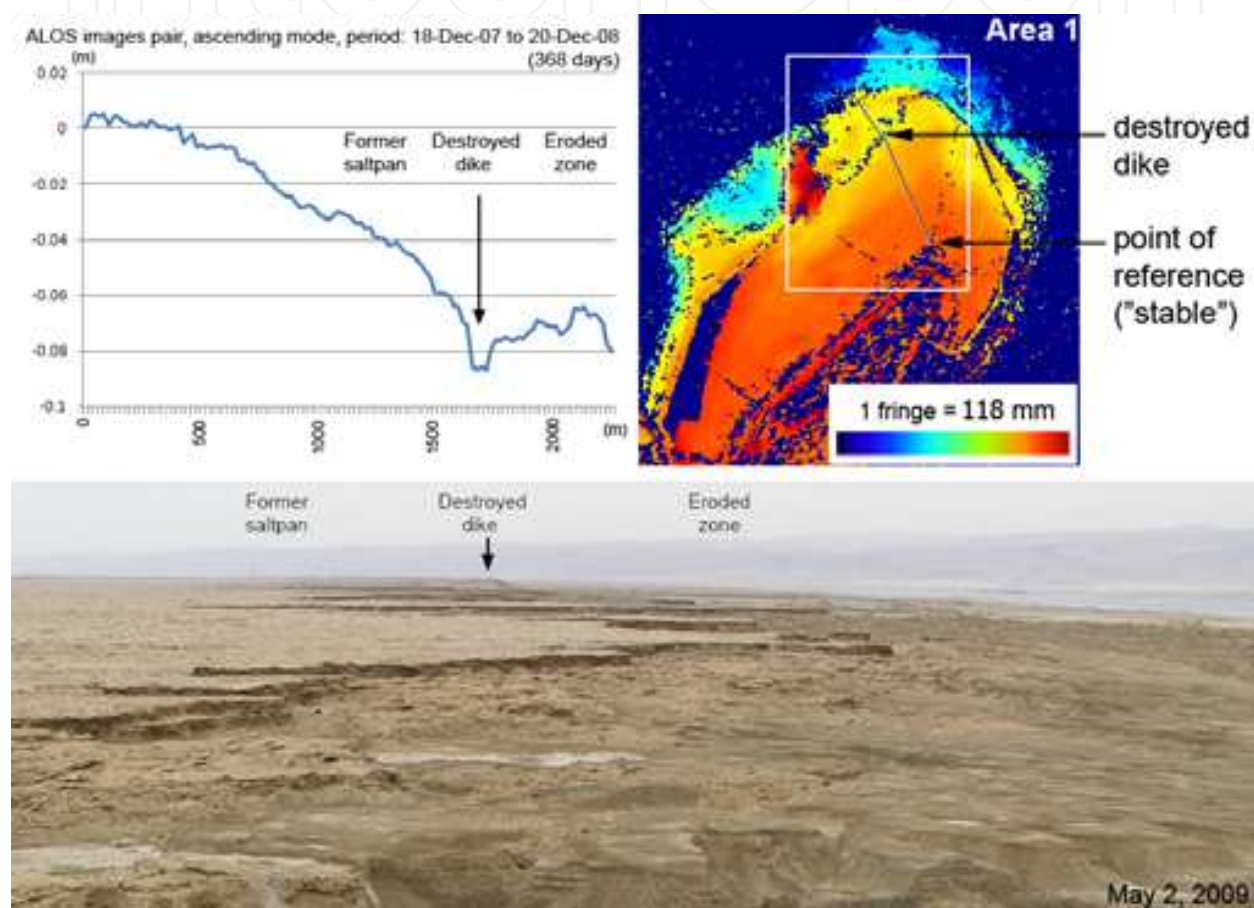


Fig. 14. Area 1 - ground movements detected by ALOS during the period of observation from 18-Dec-2007 to 20-Dec-2008. Northern Lisan, picture of the area where a dike was destroyed in March 2000 (USD 38M). View from the northern remaining dike segment toward SW direction.

The ground displacement observed are localized along coastal zones recently emerged. There, ground-water lowers following the Dead Sea level drop (Closson et al., 2007). As a consequence, salty-marls/argile compaction phenomena occur and trigger land subsidence (Baer et al., 2002). Differential land subsidence produced extensive areas of earth fissures which affect earthen dikes of the Arab Potash Company. Other effects include an increased landslide hazards (Closson et al., 2009).

Shimoni et al. (2002), Closson et al. (2003) and Closson (2005b) have shown that the northern subsidence areas are also at the periphery of rising sub-domes (e.g. cross section 3). This

geographical proximity suggested a possible connection between the two phenomena. However this assumption is not supported by the drastic increase in the subsidence rates revealed by ALOS and ENVISAT data in 2008. The increasing rate of subsidence is following a similar trend in the rate of sinkholes proliferation (Closson et al., 2010) which is connected with the Dead Sea level lowering.

## 5.2 Uplifts and subsidence in relation with the Lisan salt diapir

Cross sections 3-6 (Figure 13) illustrate the surface displacements caused by differential rising rates in the central and southern Lisan. Cross section 3 characterizes a sub-dome rising at a rate of 13 mm/year for the period of observation. It is representative of four sub-domes existing in this area (see locations on Figure 10: 735-3466, 736-3468, 736-3469, and 737-3470). At the opposite, cross section 4 and 5 characterize subsidence linear and curvilinear structural features.

Cross section 4 focuses on a linear zone oriented N-S presenting a subsidence of 14 mm/year at the intersection with another linear structure oriented E-W. The minima areas such as the one discussed here are generally surrounded by several rising sub-domes (e.g. Figure 10: yellow spots surrounding blue/cyan spots in 736/737-3461).

Cross section 5 concerns a wide sub-dome in the southern Lisan (Figure 15, inset).

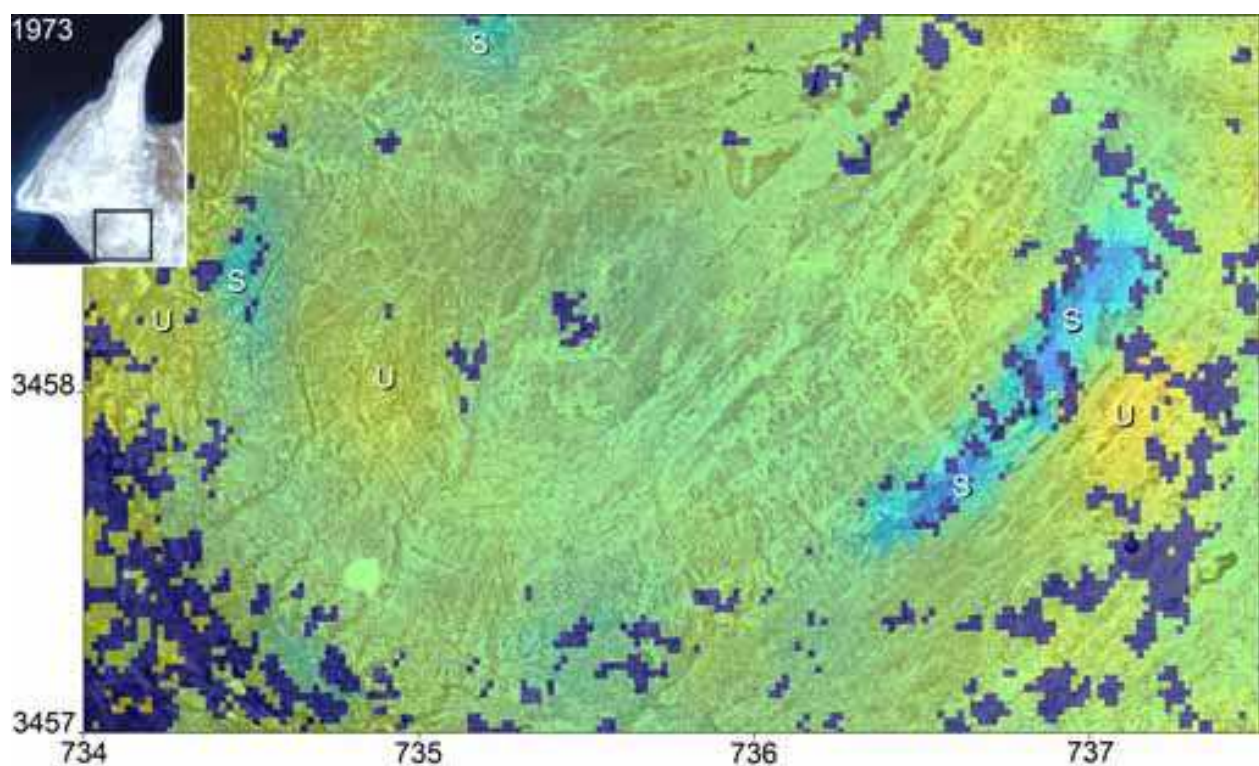


Fig. 15. Uplift and subsidence areas (U/S letters) are superimposed to a Corona image acquired on August 5, 1970. ERS interferogram covers the period 29-Jul-95 to 14-Jul-96. Dark blue pixels correspond to decorrelated areas. Inset: Landsat image of the Lisan acquired in 1973.

Background image is a high resolution Corona photograph acquired in August 5, 1970. A curvilinear structure characterized by blue colors is centered over the place of the maximum

vertical thrust (735.5-3458). Yellow and cyan/blue colors derive from the interferogram displayed in Figure 10. They correspond relatively to uplifts (U) and subsidence (S). Subsidence appears at the synclinal area between the flanks of the folds. They attest that this dome is active.

Cross section 6 (Figure 13) brings an overview of the displacement through the Lisan. At least, it illustrates the great complexity of movements affecting the sub-domes of the Lisan diapir structure. In terms of ground displacements, the surface of the salt dome can be compared as a bubbling surface. It is particularly obvious over Figure 10 while Figure 9 shows less evidence of surface displacements. When comparing displacement fields of Figure 11 and 12, one can observe respectively that the northern Lisan is uplifted over a very short period of time (35 days) and the southwestern part records most of the rise during a period of 1261 days. The variations of speeds are important in space and time. It supports the idea that the Lisan diapir uplift is episodic and not monotonous. This observation was already mentioned by Shimoni et al. (2002) and had been confirmed by the processing of ALOS and ENVISAT data for the period 2007-2008. The main ground movement activities are localized in the northern part of the Lisan (uplift) and in the southern Lynch Strait area (subsidence, Closson et al., 2010b). A possible explanation to explain this increase of activity could be that 90M cubic meters of Dead Sea brine have been introduced in 2006 in a saltpan repaired during the period 2001-2005. This load in an area recognized as relatively unstable during the 1990s, could have reactivated numbers of concealed faults and fractures.

## 6. Summary and conclusions

The problem of the measurement of ground displacements caused by the rising of a salt diapir in the region of the Lisan, Dead Sea, Jordan had been tackled by applying radar interferometry techniques to 27 satellite images acquired in 1992-1999 and 2007-2008.

Baer et al. (2002) and Shimoni et al. (2002) have studied the Lisan by applying the same techniques to 16/17 ERS images (C-band). Their work covered the period 1992-2000. Here, two additional sensors have been used: ALOS (L-band) and ENVISAT (C-band) satellites. The superimposition of radar phase images acquired by ERS, ALOS and ENVISAT satellite radar from different epochs have been compared, resulting in the precise detection of mm scale vertical changes from observed interference fringes.

The processing of ERS data led to the same conclusions than Shimoni et al. (2002). The rate of the deformation over the Lisan is irregular during the 1990s. Cross-sections have shown that the highest deformation occurred in the northern part of the peninsula, at the place where one production unit of the Arab potash Company was destroyed in March 2000. Most of the zones in subsidence are observed in the peninsula periphery while the main uplifted areas are located in the central and southern parts.

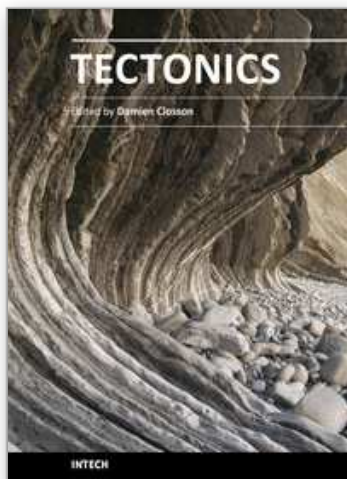
The comparison with the measures realized with the dataset of 2007-2008 shows a drastic increase in the rate of subsidence at the periphery of the area of interest. The rising of the northern part of the peninsula is more pronounced than the one of the south and central parts. ALOS data revealed that the most active part during the period 2007-2008 was located in the Lynch Strait area. The use of L-band sensor allows the detection of ground displacements leading to decorrelation in C-band and C-band preserve coherence in places where L-band decorrelate due to specular reflection.

## 7. References

- Abou Karaki, N. (1987). *Synthèse et carte sismotectonique des pays de la bordure de la Méditerranée: sismicité du système de faille du Jourdain - Mer Morte*. Université Louis Pasteur, Strasbourg, France.
- Al-Zoubi, A. & ten Brink, U.S. (2001). Salt Diapir in the Dead Sea and their Relationship to Quaternary Extensional Tectonics. *Marine and Petroleum Geology*, 18, 7, August 2001 779-797, ISSN: 0264-8172.
- Arieh, E.; Rotstein, Y. & Peled, U. (1982). The Dead Sea Earthquake of April 1979. *Bulletin of the Seismological Society of America*, 72, 5, October 1982, 1627-1634, ISSN: 0037-1106.
- Baer, G.; Schattner, U.; Wachs, D.; Sandwell, D.; Wdowinski, S. & Frydman, S. (2002). The Lowest Place on Earth is Subsiding - An InSAR (Interferometric Synthetic Aperture Radar) Perspective. *Geological Society of America Bulletin*, 114, 1, January 2002, 12-23. ISSN: 0016-7606.
- Bartov, Y. (1999). *The Geology of the Lisan Formation in Massada Plain and the Lisan Peninsula*. The Hebrew University of Jerusalem, Israel.
- Bartov, Y.; Stein, M.; Enzel, Y.; Agnon, A.; Reches, Z. (2002). Lake-levels and sequence stratigraphy of Lake Lisan, the late Pleistocene precursor of the Dead Sea. *Quaternary Research*, 57, 1, January 2002, 9-21, ISSN: 0033-5894.
- Bartov, Y. (2004a). Paleolakes at the Dead Sea basin. Chapter 2. In: *Fungal life in the Dead Sea (Biodiversity of cyanoprokaryotes, algae and fungi of Israel)*, Nevo, E., Oren, A., Wasser, S., (Ed). Gantner Verlag, 325 pp, ISBN: 3-906166-10-4.
- Bartov, Y. (2004b). *Sedimentary fill analysis of a continental basin—the Late Pleistocene Dead Sea*. Ph.D. thesis, Hebrew University, Jerusalem.
- Bartov, Y. & Sagy, A. (2004). Late Pleistocene extension and strike-slip in the Dead Sea. *Geological Magazine*, 141, 5, September 2004, 565-572. ISSN: 0016-7568.
- Bartov, Y. ; Enzel, Y. ; Stein, M. ; Agnon, A. (2004). Transgressional erosion - implication on the Holocene uplift rate of the Lisan diapir. *Geological Society of Israel Annual Meeting*, Abstracts, p. 12.
- Bartov, Y.; Agnon, A.; Enzel, Y. & Stein, M. (2006). Late Quaternary faulting and subsidence in the central Dead Sea basin. *Israel Journal of Earth Sciences*, 55, 1, 18-31, ISSN: 0021-2164.
- Ben-Avraham, Z. (1997). Geophysical Framework of the Dead Sea: Structure and Tectonics, In: *The Dead Sea, the Lake and its Setting*, Niemi T.M., Ben-Avraham Z., Gat J. (Ed), 22-35, Oxford University Press, ISBN-10: 0195087038, ISBN-13: 978-0195087031, USA.
- Ben-Avraham, Z. & Lazar, M. (2006). The structure and development of the Dead Sea basin: recent studies. In: *New frontiers in Dead Sea paleoenvironmental research: Geological Society of America Special Paper 401*, Enzel, Y., Stein, M., Agnon, A., (Ed.), 1-13, Geological Society of America Special Papers, ISBN 0-8137-2401-5, Boulder CO.
- Bender, F.K. (1974). *Geology of Jordan* (supplementary edition of volume 7). Gebrüder Borntraeger, ISBN: 3-443-11707-4, Berlin-Stuttgart, Germany.
- Closson, D.; Abou Karaki, N.; Hansen, H.; Derauw, D.; Barbier, C. & Ozer, A. (2003a). Space-borne Radar Interferometric Mapping of Precursory Deformations of a Dyke Collapse - Dead Sea Area - Jordan. *International Journal of Remote Sensing*, 24, 4, February 2003, 843-849, ISSN 0143-1161.

- Closson, D.; Abou Karaki, N.; Hussein, M. J.; Al-Fugha, H.; Ozer, A. & Mubarak, A. (2003b). Subsidence and Sinkholes along the Jordanian Coast of the Dead Sea: Contribution of Gravimetry and Radar Differential Interferometry. *Comptes Rendus Geosciences*, 335, 12, October 2003, 869-879, ISSN 1631-0713.
- Closson, D.; Abou Karaki, N.; Klinger, Y. & Hussein, M.J. (2005). Subsidence Hazards Assessment in the Southern Dead Sea Area, Jordan. *Pure and Applied Geophysics*, 162, 2, 221-248, ISSN 0033-4553.
- Closson, D. (2005a). Structural Control of Sinkholes and Subsidence Hazards along the Jordanian Dead Sea Coast. *Environmental Geology*, 47, 2, 290-301, ISSN: 0943-0105.
- Closson, D. (2005b). *Cooccurrence between the Geo-Hazards Induced by the Dead Sea Level Lowering and the Geological Setting – Lisan Peninsula, Lynch Strait, Ghor Al Haditha – Jrdan*. PhD Thesis, University of Liege, Belgium.
- Closson, D.; LaMoreaux, P.E.; Abou Karaki, N. & Al-Fugha, H. (2007). Karst system developed in salt layers of the Lisan Peninsula, Dead Sea, Jordan. *Environmental Geology*, 52, March 2007, 155-172, ISSN: 0943-0105.
- Closson, D. & Abou Karaki, N. (2009a). Human-induced geological hazards along the Dead sea coast. *Environmental Geology – Special Issue*, 58, 2, July 2009, 371-380, ISSN: 0943-0105.
- Closson, D. & Abou Karaki, N. (2009b). Salt karst and tectonics: sinkholes development along tension cracks between parallel strike-slip faults, Dead Sea, Jordan. *Earth Surface Processes and Landforms*, 34, August 2009, 1408-1421. ISSN: 0197-9337.
- Closson, D.; Abou Karaki, N. & Hallot, F. (2010a). Landslides along the Jordanian Dead Sea coast triggered by the lake level lowering. *Environmental Earth Sciences*, 94, February 2010, 1417-1430, ISSN: 1866-6280.
- Closson, D.; Abou Karaki, N.; Milisavljević, N.; Hallot, F. & Acheroy, M. (2010b). Salt-dissolution-induced subsidence in the Dead Sea area detected by applying interferometric techniques to ALOS Palsar Synthetic Aperture Radar images. *Geodinamica Acta*, 23, 65-78. ISSN: 0985-3111.
- Derauw, D. (1999). *Phasimétrie radar à synthèse d'ouverture: théorie et applications*. PhD Thesis, University of Liege, Belgium..
- Diabat, A.A. (2005). Sinkholes related to Tectonic Factor at Ghor Al Haditha Area, Dead Sea/Jordan. *Hydrogeologie und Umwelt*, 33, 1-17, ISSN 09309- 3757.
- Ferry, M.; Meghraoui, M.; Abou Karaki, N.; Al-Taj, M.; Amoush, H.; Al-Dhaisat, S. & Barjous, M. (2007). A 48-kyr-long slip rate history for the Jordan Valley segment of the Dead Sea Fault. *Earth and Planetary Science Letters*, 260, 3-4, 30 August 2007, 394-406, ISSN 0012-821X.
- Freund, R.; Zak, I. & Garfunkel, Z. (1968). Age and Rate of the Sinistral Movement along the Dead Sea Rift. *Nature*, 220, 19 October 1968, 253 – 255, ISSN : 0028-0836.
- Freund, R.; Garfunkel, Z.; Zak, I.; Goldberg, M.; Weisbrod, T. & Derin, B. (1970). The Shear along the Dead Sea Rift. *Philosophical Transactions Royal Society London*, 267, 29 October 1970, 107-130, ISSN: 0080-4614.
- Gardosh, M.; Reches, Z. & Garfunkel, Z. (1990). Holocene Tectonic Deformation along the Western Margins of the Dead Sea. *Tectonophysics*, 180, 123-137, ISSN: 0040-1951.
- Gardosh, M.; Kashai, E.; Salhov, S.; Shulman, H. & Tannenbaum, E. (1997). Hydrocarbon Exploration in the Southern Dead Sea Area, In: *The Dead Sea, The Lake and its Setting*,

- Niemi T.M., Ben-Avraham Z., Gat J. (Ed). 57-72, Oxford University Press, ISBN-10: 0195087038, ISBN-13: 978-0195087031, USA.
- Garfunkel, Z.; Zak, I. & Freund, R. (1981). Active Faulting in the Dead Sea Rift. *Tectonophysics*, 80, 1-4, 10 December 1981, 1-26, ISSN: 0040-1951.
- Garfunkel, Z. & Ben Avraham, Z. (1996). The Structure of the Dead Sea Basin. *Tectonophysics*, 266, 1-4, 15 December 1996, 155-176, ISSN: 0040-1951.
- Garfunkel, Z. (1997). The History and Formation of the Dead Sea Basin, In: *The Dead Sea, the Lake and its Setting*, Niemi T.M., Ben-Avraham Z., Gat J. (Ed), 36-55, Oxford University Press, ISBN-10: 0195087038, ISBN-13: 978-0195087031, USA.
- Ginat, H.; Enzel, Y. & Avoni, Y. (1998). Translocated Plio-Pleistocene Drainage Systems Along the Arava Fault of the Dead Sea Transform. *Tectonophysics*, 284, 1-2, 15 January 1998, 151-160, ISSN: 0040-1951.
- Hall J.K. (1997). Topography and Bathymetry of the Dead Sea Depression, In: *The Dead Sea, the Lake and its Setting*, Niemi T.M., Ben-Avraham Z., Gat J. (Ed), 11-21, Oxford University Press, ISBN-10: 0195087038, ISBN-13: 978-0195087031, USA.
- Klinger, Y.; Avouac, J.P.; Abou Karaki, N.; Dorbath, L.; Bourles, D. & Reyss, J.L. (2000). Slip-Rate on the Dead Sea Transform Fault In Northern Araba Valley (Jordan). *Geophysical Journal International* 142, 3, September 2000, 755-768, ISSN 0956-540X .
- Neev, D. & Emery, K.O. (1967). The Dead Sea – Depositional Processes and Environments of Evaporates. *Geological Survey of Israel Bulletin*, 41, 1-147.
- Niemi, T.; Zhang, H.; Atallah, M. & Harrison, J.B. (2001). Late Pleistocene and Holocene Slip Rate of the Northern Wadi Araba Fault, Dead Sea Transform, Jordan. *Journal of Seismology*, 5, 3, 449-474, ISSN: 1383-4649.
- Pe'eri, S.; Wdowinski, S.; Shtibelman, A.; Bechor, N.; Bock, Y.; Nikolaidis, R. & Van Domselaar, M. (2002). Current Plate Motion across the Dead Sea Fault from three Years of Continuous GPS Monitoring. *Geophysical Research Letter*, 29, 14, 26 July 2002, 42/1 – 42/4, ISSN 0094-8276.
- Quennell, A. (1958). The Structural and Geomorphic Evolution of the Dead Sea Rift. *Quarterly journal of the Geological Society of London*, 114, 1-4, 1-24, ISSN 0016-7649.
- Shimoni, M.; Hanssen, R.F.; Van Der Meer, F.; Kampes, B.M. & Ben Dor, E. (2002). Salt Diapir Movements Using SAR Interferometry in the Lisan Peninsula, Dead Sea Rift. *Proceedings of SPIE* , pp. 151-160, ISBN 0-8194-4268-2, Toulouse, September 17-18, 2001, SPIE, Bellingham WA, USA.
- Sunna, B.F. (1986). The Geology of Salt Deposits in the Lisan Peninsula-Dead Sea. *Seminar on salt in the Arab World*, Ministry of Energy and Mineral Resources, Natural Resources Authorities, May 4-6, 1986, Amman, Jordan.
- Weinberger, R.; Begin, Z.B.; Waldmann, N.; Gardosh, M.; Baer, G.; Frumkin, A. & Wdowinski, S. (2006). Quaternary rise of the Sedom diapir, Dead Sea basin. In: *New frontiers in Dead Sea paleoenvironmental research: Geological Society of America Special Paper 401*, Enzel, Y., Stein, M., Agnon, A., (Ed.), 33-51, Geological Society of America, , ISBN 0-8137-2401-5, Boulder CO.
- Zak, I. (1967). *The Geology of Mount Sedom*. Hebrew University of Jerusalem, Jerusalem, Israel.



## **Tectonics**

Edited by Dr. Damien Closson

ISBN 978-953-307-545-7

Hard cover, 358 pages

**Publisher** InTech

**Published online** 28, February, 2011

**Published in print edition** February, 2011

The term tectonics refers to the study dealing with the forces and displacements that have operated to create structures within the lithosphere. The deformations affecting the Earth's crust are result of the release and the redistribution of energy from Earth's core. The concept of plate tectonics is the chief working principle. Tectonics has application to lunar and planetary studies, whether or not those bodies have active tectonic plate systems. Petroleum and mineral prospecting uses this branch of knowledge as guide. The present book is restricted to the structure and evolution of the terrestrial lithosphere with dominant emphasis on the continents. Thirteen original scientific contributions highlight most recent developments in seven relevant domains: Gondwana history, the tectonics of Europe and the Near East; the tectonics of Siberia; the tectonics of China and its neighbourhood; advanced concepts on plate tectonics are discussed in two articles; in the frame of neotectonics, two investigation techniques are examined; finally, the relation between tectonics and petroleum researches is illustrated in one chapter.

### **How to reference**

In order to correctly reference this scholarly work, feel free to copy and paste the following:

Damien Closson, Najib Abou Karaki, Nada Milisavljević, Frédéric Hallot, and Marc Acheroy (2011). Salt Tectonics of the Lisan Diapir Revealed by Synthetic Aperture Radar Images, *Tectonics*, Dr. Damien Closson (Ed.), ISBN: 978-953-307-545-7, InTech, Available from: <http://www.intechopen.com/books/tectonics/salt-tectonics-of-the-lisan-diapir-revealed-by-synthetic-aperture-radar-images>

**INTECH**  
open science | open minds

### **InTech Europe**

University Campus STeP Ri  
Slavka Krautzeka 83/A  
51000 Rijeka, Croatia  
Phone: +385 (51) 770 447  
Fax: +385 (51) 686 166  
[www.intechopen.com](http://www.intechopen.com)

### **InTech China**

Unit 405, Office Block, Hotel Equatorial Shanghai  
No.65, Yan An Road (West), Shanghai, 200040, China  
中国上海市延安西路65号上海国际贵都大饭店办公楼405单元  
Phone: +86-21-62489820  
Fax: +86-21-62489821

© 2011 The Author(s). Licensee IntechOpen. This chapter is distributed under the terms of the [Creative Commons Attribution-NonCommercial-ShareAlike-3.0 License](https://creativecommons.org/licenses/by-nc-sa/3.0/), which permits use, distribution and reproduction for non-commercial purposes, provided the original is properly cited and derivative works building on this content are distributed under the same license.

IntechOpen

IntechOpen